# A finite-strain thermomechanical behavior model for iron-based shape memory alloys accounting for coupling between phase transformation and plastic slip

Achref Sallami[a], Walid Khalil[b], Tarak Bouraoui[a], Tarak Ben Zineb[c],*

[a] Université de Monastir, École Nationale d'Ingénieurs de Monastir, LGM, LR99ES32, TN, 5000, Monastir, Tunisia
[b] Université de Gabès, Institut Supérieur des Systèmes Industriels de Gabès, TN, 6032, Gabès, Tunisia
[c] Université de Lorraine, CNRS, Arts et Métiers ParisTech, LEM3, F-54000, Nancy, France

ABSTRACT

Shape Memory Alloys (SMAs) have the main interesting property to recover an inelastic strain induced by martensitic transformation. The initial shape can be recovered directly after unloading or with the application of an additional heating. Iron-based SMAs (Fe-SMAs) are characterized by a high coupling between phase transformation and plastic slip at low temperatures under small stress levels. Thermomechanical constitutive models describing such coupling developed based on small-strains are not suitable for higher loading levels. This motivates the proposed development of a finite-strain constitutive model for Fe-SMAs considering thermomechanical coupling between phase transformation and plastic slip, and by extending the small-strain model within a finite-strain thermodynamical framework in order to describe large strains mainly induced by plastic hardening in Fe-SMA material point. The model here has two internal variables (volume fraction of martensite and the accumulative plastic strain). It is based on the assumption of the local multiplicative split of the deformation gradient into elastic and inelastic parts with a total Lagrangian formulation. The inelastic deformation gradient splits also into a transformation and a plastic parts. The developed model is implemented into the commercial software Matlab. The results obtained for thermomechanical loadings are discussed and, a good agreement with experimental results is also observed.

## 1. Introduction

Conventional materials have long been used for their structural properties. However, continuous technological innovation in advanced fields such as aeronautics, bio-medical, energy production and automotive, as well as the progress made over the few decades in the development of materials with high multiphysical coupling have led to fulfill other functionalities such as sensing, actuation, etc. In this category of so-called functional, adaptive or intelligent materials, the most widely used materials are those having electrical/mechanical (piezoelectric), magnetic/mechanical (magnetostrictive) or thermal/mechanical (shape memory alloys) coupling (e.g. Kim and Kwon (2015); Ojha and Sehitoglu (2016); Lookman et al. (2017); Xue et al. (2018); Jella et al. (2019)).

The evolution of research on Shape Memory Alloys (SMAs) allowed to better understand the physical mechanisms as the phase transformation and plastic slip occurring on the microstucture, leading to innovative industrial applications. The latter have main

---

characteristics known as the shape memory effect and the pseudo-elasticity (super-elasticity). In the past, many studies have been undertaken making it possible to modelize and characterize the behaviors of these alloys both metallurgically and thermo-mechanically (e.g. Christ and Reese (2009); Xiao (2014); Cissé et al. (2016a, b); Xu et al. (2018)).

Three SMAs families are currently used: Copper-based SMAs (Cu–Al–Be, Cu–Zn–Al, etc.), Nickel–Titanium-based SMAs (Ni–Ti, Ni–Ti– Nb, etc.) and Iron-based SMAs (Fe–Mn–Si, Fe–Ni–Co, etc.). In particular, Iron-based SMAs (Fe-SMAs) are distinguished from other SMAs by their thermomechanical coupling between martensitic transformation and plastic slip. Koval et al. (1979) noticed a shape memory effect on Fe–Ni–Co–Ti steel. The discovery of this new material was better recognized after the research of Sato et al. (1982) on Fe–Mn–Si that reveals the same shape memory effect. Since then these new materials have been recognized by the name Iron-based SMAs. Fe-SMAs drew a lot of attention for their use of various applications due to their low cost and their good mechanical properties. The shape memory effect in the case of the Fe-SMAs comes, on the one hand, from the mechanically induced phase transformation, from the γ -austenite FCC phase to the ε-martensite HCP phase, and, on the other hand, from the reverse transformation activated only by heating. More studies have been carried out on the phase transformation behavior (Kokorin et al., 1993), the plastic slip behavior (Bouraoui et al., 2008; Khalil et al., 2013), the rubber effect (Torra et al., 2015), the pseudo-elasticity (Sawaguchi et al., 2005), the physical properties (Lin and Lin, 1996) and the improvement of the shape memory effect (Wang et al., 2016; Mamivand et al., 2014). The non-Schmid effect, well known for Ni–Ti and Cu-based SMAs (Alkan et al., 2018; Alkan and Sehitoglu, 2017, 2019), is less noticeable at the macroscopic scale for Fe-SMAs. In fact, the difference between tension and compression in phase transformation and the hardening anisotropy are much less pronounced in Fe-SMAs (Cao and Iwamoto, 2019; Nishimura et al., 1996, 1997b).

Unlike NiTi and Cu-based SMAs, very few constitutive models are available for Fe-SMAs. The modeling of these materials has attracted many researchers leading to relatively large number of studies (Nishimura et al. (1997a); Nishimura and Tanaka (1998); Goliboroda et al. (1999); Nishimura et al. (2003); Jemal et al. (2009); Khalil et al. (2012); Cissé et al. (2017)). Jemal et al. (2009) constructed the first three-dimensional model describing the thermomechanical behavior of Fe-SMAs. This model is based on the description of a macroscopic behavior of a representative volume element (RVE). They defined the accumulative plastic strain γ with the martensite volume fraction χ as the internal variables and the stress Σ with the temperature $T$ as controlling variables. The expression of the Gibbs free energy is assumed taking into account of the phase transformation, the plastic slip and the interaction energies leading to linear hardening. Khalil et al. (2012) developed a model using a thermodynamic/energetic approach while retaining the same internal variables as the model of Jemal et al. (2009). It rectifies this latter by introducing a loading function for the reverse phase transformation. They Modified the yield force of plasticity by considering the temperature dependence, and improved the description of inter-granular and intra-granular interactions to predict the experimentally observed non linear hardening. More recently, Cissé et al. (2017) introduced a new model for Fe-SMAs based on the Zaki and Moumni (2007) model for NiTi SMAs, and presented an energetic formulation. The Helmholtz free energy Φ is written as a function of that in the austenite, $\Phi_a$, martensite, $\Phi_m$, and an interaction energy, $\Phi_{int}$ introduced by $\Phi = (1 − \xi)\Phi_a + \xi\Phi_m + \Phi_{int}$, with ξ being the volume fraction of martensite. All these constitutive models were built assuming the small-strain. However, Fe-SMAs can reach large strain levels because of their ductility. Therefore, a small-strain formulation may not be suitable, and it is necessary to account for the evolution of the deformed configuration during loading. This motivates the present authors to develop a finite-strain behavior law for Fe-SMAs.

Plastic slip coupled or uncoupled with respect to phase transformation, could lead to large inelastic strains in ductile metals and alloys as TRansformation Induced Plasticity (TRIP) (Wei et al., 2007) and TWinning Induced Plasticity (TWIP) (Kalsar and Suwas, 2017) steels and also Fe-SMAs (Wen et al., 2014). This motivated the application of the finite strain formulation for the conventional elasto-plastic material behavior modeling. The basic equations for the mechanics of solids in finite strains can be found in many references. Among these references (Taylor, 1938); (Malvern, 1969); (Lion, 2000); (Sidoroff and Dogui, 2001). The finite strain plasticity formulation is a difficult and controversial topic, both conceptually and technically (Sidoroff and Dogui, 2001). The starting point of this formulation can be a multiplicative decomposition. The total deformation gradient **F** breaks down as $\mathbf{F} = \mathbf{F}_{el}\mathbf{F}_{pl}$, with $\mathbf{F}_{el}$ and $\mathbf{F}_{pl}$ representing the elastic and plastic deformation gradients (Lee, 1969); (Sidoroff and Dogui, 2001); (Vladimirov et al., 2010); (Grilo et al., 2016). Finite strain models are developed either for the classical SMAs or to TRIP and TWIP steels. Beginning with the classical SMAs, in literature, a large number of models have been proposed. The work of Christ and Reese (2009) dealt with two typical and important phenomenon of SMA behavior: Pseudo-Elasticity (PE) and Shape Memory Effect (SME). As in classical plasticity, an unconstrained intermediate state decouples the elastic deformation gradient of the deformation gradient that are induced by phase transformation $\mathbf{F}_t = \mathbf{F}_\varepsilon^{-1}\mathbf{F}$ (Christ and Reese, 2009). Evangelista et al. (2009) proposed a phenomenological model in finite transformations for SMAs describing PE and SME behavior. It model was based on a local multiplicative formulation of the deformation gradient into an elastic part and a phase transformation part $\mathbf{F} = \mathbf{F}_e\mathbf{F}_t$. Constitutive model equations were written with respect to the undeformed configuration (Lagrangian approach). Arghavani et al. (2011) developed a finite strain three-dimensional Hencky-based kinematic-hardening constitutive model. They introduced the decomposition of the deformation gradient like that of Evangelista et al. (2009). More recently, Wang et al. (2017) constructed a finite strain constitutive model for SMAs that takes into account of thermomechanical coupling activation and reorientation of martensite by extending the small-strain model of Zaki and Moumni (2007). To further explain the thermomechanical coupling, Wang et al. (2017) decomposed the total deformation gradient **F** into, elastic $\mathbf{F}_e$, inelastic (transformation) $\mathbf{F}_{ine}$ and thermal $\mathbf{F}_\theta$ elements introduced by $\mathbf{F} = \mathbf{F}_e\mathbf{F}_{ine}\mathbf{F}_\theta$, inspired from the previous work of Levitas (1998). The phase transformation of the austenitic state to the martensitic state takes place in the so-called austenitic steels (Hallberg et al., 2007). It treats a finite strain model for the austenitic steel with phase transformation and it treats the phase transition through an internal variables (the phase fraction). The local multiplicative decomposition of the total deformation gradient **F** has been splitted into elastic $\mathbf{F}_e$ and irreversible $\mathbf{F}_{ir}$ parts, expressed as $\mathbf{F} = \mathbf{F}_e\mathbf{F}_{ir}$. The related physical phenomena of the TRIP steels are detailed in the review paper (Fischer et al., 2000). In Tjahjanto et al. (2008), a micromechanics-based model is highlighted and it

is formulated within a finite strain framework. The kinematic description inside a single-crystal grain of austenite was introduced by the multiplicative decomposition of the total deformation gradient $\mathbf{F}$ through elastic $\mathbf{F}_e$, plastic $\mathbf{F}_p$, and transformation $\mathbf{F}_{tr}$ parts as $\mathbf{F} = \mathbf{F}_e \mathbf{F}_p \mathbf{F}_{tr}$. Mahnken et al. (2012) presented a finite strain macroscopic material model which predicts TRIP steel behavior on the hybrid-forming process cases. Another model was developed by Mahnken et al. (2013) treating the strain-rate and temperature-dependent asymmetric plastic material behavior accompanied by phase transformation. The total deformation gradient splits multiplicatively as $\mathbf{F} = \mathbf{F}_{iso} \mathbf{F}_{vol} = \mathbf{F}_{iso}^e \mathbf{F}_i \mathbf{F}_{vol}$. Here, $\mathbf{F}_{iso}$, $\mathbf{F}_{iso}^e$, $\mathbf{F}_i$ and $\mathbf{F}_{vol}$ represent, respectively, the deformation gradient of, isochoric, elastic isochoric, irreversible, and volumetric parts. This model enhaces that of Mahnken et al. (2012) as it is built and specialized in TRIP-steels production processes.

Based on the models discussed in finite strains describing the phenomena of phase transformation and plasticity, a specific finite strain model adapted to Fe-SMAs thermomechanical behavior is detailed in this paper. Determining the behavior laws of Fe-SMAs requires a good knowledge of kinematics and the evolution laws of martensitic transformation and plasticity. This work is an extension of the Khalil et al. (2012) small-strain behavior law with some enhancement. The Helmholtz free energy is been used to describe the thermodynamic framework, and modified the driving and yield forces. An alternative multiplicative decomposition of the deformation gradient is introduced, in which the total deformation gradient $\mathbf{F}$ was first split into elastic $\mathbf{F}_{el}$ and inelastic $\mathbf{F}_{ine}$ parts. The inelastic part was then decomposed into contributions for phase transformation $\mathbf{F}_{tr}$ and plastic slip $\mathbf{F}_{pl}$. The model constitutive equations are implemented in Matlab software. Obtained results are compared to the experimental data and numerical results of Khalil et al. (2012, 2013). Results of the comparison shows the relevance of the proposed model.

Section 2, presents an overview of the basic kinematic framework introducing the adopted local decomposition of the gradient deformation. Section 3 is dedicated to the development of the constitutive model, beginning with the definition of the Helmholtz free energy and the inner potential energy to construct the Lagrangian. Then using the second law of thermodynamics, the loading functions were defined for each behavior. A solution algorithm is proposed in section 4 to explain the numerical implementation. A comparison with experimental data is performed in section 5 by adding some finite strain simulations to predict an Fe-SMA response for higher strain level. The last section 6 gives a conclusion regarding this work and some prospects.

## 2. Kinematic framework

### 2.1. Deformation gradient

The local decomposition of the deformation gradient $\mathbf{F}$ leads to two parts: an elastic part $\mathbf{F}_{el}$ defined with respect to the intermediate configuration, and an inelastic part, $\mathbf{F}_{ine}$, defined with respect to the reference configuration. The latter, in the case of Fe-SMAs, is decomposed into phase transformation induced part $\mathbf{F}_{tr}$ and a plastic induced part $\mathbf{F}_{pl}$, Fig. 1-(a).

$$\mathbf{F} = \mathbf{F}_{el}\mathbf{F}_{ine} = \mathbf{F}_{el}\mathbf{F}_{tr}\mathbf{F}_{pl} \tag{1}$$

The phase transformation-plasticity evolution diagram of yield stresses as a function of temperature (Olson and Cohen, 1972); (Bouraoui et al., 2008), describes the behavior of Fe-SMAs. Two domains are differentiated by the temperature $T_0$ (labeled $\mathbf{Ms}^\sigma$ in Bouraoui et al. (2008)) as shown in Fig. 1-(b). If the temperature of the material is lower than the temperature $T_0$, the phase transformation of the austenite to martensite has priority. Otherwise, the activation of the plasticity in the austenite takes place, preventing the nucleation of the martensite.
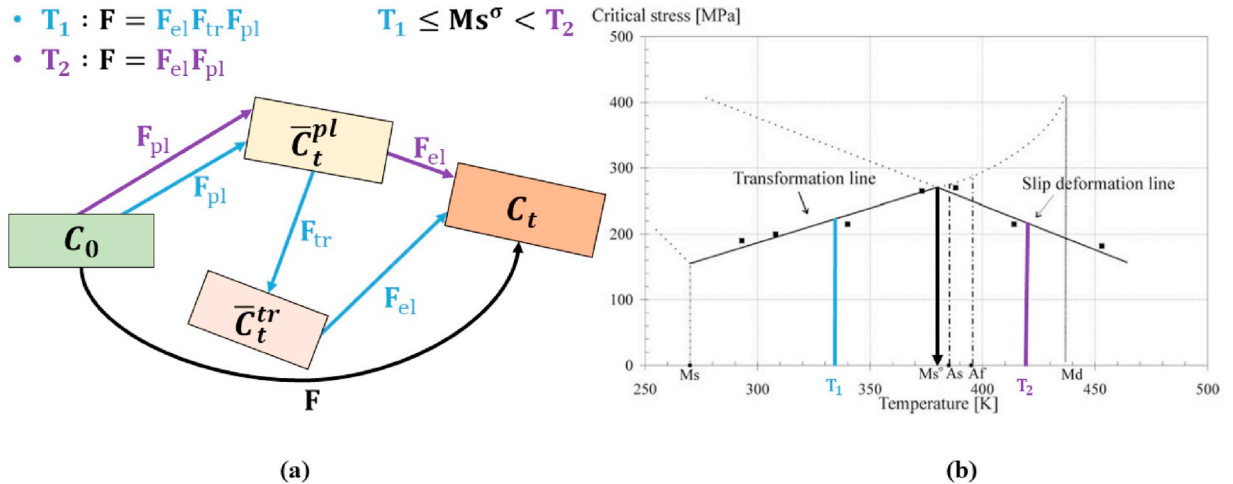


Fig. 1. (a) Decomposition of deformation gradients; (b) Stress-Temperature diagram for phase transformation and plasticity (Bouraoui et al., 2008).

### 2.2. Strain tensors and their time derivatives

The deformation gradient $\mathbf{F}$ is not a suitable strain measure. Therefore, a Green-Lagrange strain $\mathbf{E}$ tensor was adopted to quantify the local strain in a given material point. It is defined as follows:

$$\mathbf{E} = \frac{1}{2}(\mathbf{C} - \mathbf{I}) \tag{2}$$

where $\mathbf{C} = \mathbf{F}^T\mathbf{F}$ denotes the right Cauchy-Green tensor, and $\mathbf{I}$ the second order identity tensor. Similarly, the elastic Cauchy-Green tensor is defined as:

$$\mathbf{C}_{el} = \mathbf{F}_{el}^T\mathbf{F}_{el} = \mathbf{F}_{ine}^{-T}\mathbf{C}\mathbf{F}_{ine}^{-1} \tag{3}$$

Moreover, the velocity gradient $\mathbf{L} = \frac{\partial \dot{u}}{\partial x}$ is decomposed into a, symmetric part $\mathbf{D}$ and antisymmetric part $\mathbf{W}$ defined as follow:

$$\mathbf{L} = \dot{\mathbf{F}}\mathbf{F}^{-1} = \mathbf{D} + \mathbf{W}; \quad \begin{cases} \mathbf{D} = \frac{1}{2}(\mathbf{L} + \mathbf{L}^T) \\ \mathbf{W} = \frac{1}{2}(\mathbf{L} - \mathbf{L}^T) \end{cases} \tag{4}$$

According to (2), the time derivative of the Green-Lagrange strain tensor (Green-Lagrange strain rate) can be calculated as.

$$\dot{\mathbf{E}} = \frac{1}{2}\dot{\mathbf{C}} = \frac{1}{2}(\dot{\mathbf{F}}^T\mathbf{F} + \mathbf{F}^T\dot{\mathbf{F}}) \tag{5}$$

Using (4), the Green-Lagrange strain rate can be rewritten as:

$$\dot{\mathbf{E}} = \frac{1}{2}\mathbf{F}^T(\mathbf{L} + \mathbf{L}^T)\mathbf{F} = \mathbf{F}^T\mathbf{D}\mathbf{F} \tag{6}$$

For further use, the time derivative of the elastic right Cauchy–Green tensor has been defined as follows:

$$\dot{\mathbf{C}}_{el} = -\mathbf{L}_{ine}^T\mathbf{C}_{el} + \mathbf{F}_{ine}^{-T}\dot{\mathbf{C}}\mathbf{F}_{ine}^{-1} - \mathbf{C}_{el}\mathbf{L}_{ine} \tag{7}$$

with $\mathbf{L}_{ine} = \mathbf{L} - \mathbf{L}_{el}$ being the inelastic velocity gradient.

## 3. Fe-SMA thermomechanical constitutive model in finite strains

### 3.1. Free energy function

To satisfy the principle of material objectivity, it is assumed that the Helmholtz free energy $\Psi$ depends on the elastic right Cauchy-Green strain tensor $\mathbf{C}_{el}$, the martensite volume fraction $\chi$, the plastic slip $\gamma$, and the temperature $T$. The Helmholtz free energy of a Fe-SMA is the sum of hyper-elastic and inelastic energies as:

$$\Psi = \Psi(\mathbf{C}_{el}) + \Psi(\chi, \gamma, T) \tag{8}$$

The hyper-elastic energy can be defined as (Wang et al., 2017):

$$\Psi(\mathbf{C}_{el}) = \frac{\mu}{2}\left(I_{\mathbf{C}_{el}} - 3\right) - \mu \ln J + \frac{\lambda}{2}(\ln J)^2 \tag{9}$$

where $\mu$ and $\lambda$ are equivalent Lamé constants by assuming an isotropic elastic behavior with the same properties at the martensitic and austenitic states. $I_{\mathbf{C}_{el}}$ is the first cauchy invariant of $\mathbf{C}_{el}$ and $J = det(\mathbf{F})$ is the deformation Jacobian (third invariant of $\mathbf{F}$). The inelastic behavior of Fe-SMAs is induced by phase transformation and plastic slip for a given poly-crystalline RVE (Fig. 2).

By considering the macroscopic induced effective behavior of this RVE, starting from local micro-mechanical description, a corresponding inelastic free energy is derived. All these steps leading to the adopted constitutive model are detailed in Khalil et al. (2012) for small strain case:
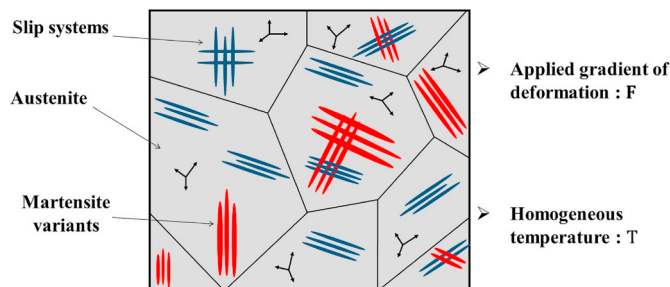


**Fig. 2.** Representative volume element of an Fe-SMA.

$$\Psi(\chi, \gamma, T) = c_v \left[ (T - T_0) - T \ln\left(\frac{T}{T_0}\right) \right] + B(T - T_0)\chi + G_g(\mathbf{E}_{ine})$$
$$+ [G_v(\chi) + (1 - \chi)G_s(\gamma) + G_{sv}(\gamma, \chi)] \tag{10}$$

where $T$ is the current temperature, $c_v$, $B$, and $T_0$ are the material parameters, $G_g(\mathbf{E}_{ine})$ is the intergranular interaction energy and $G_v$, $G_s$, $G_{sv}$ are, respectively, the interaction functions between martensite variants, between plastic slip system, and between martensite variants and plastic slip systems. They are defined as follows:

$$G_g(\mathbf{E}_{ine}) = \frac{H_g}{(n_g + 1)}(\mathbf{E}_{ine} : \mathbf{E}_{ine})^{n_g + 1} \tag{11}$$

$$G_v(\chi) = \frac{H_v}{n_v + 1}\chi^{n_v + 1} \tag{12}$$

$$G_s(\gamma) = \frac{H_s}{n_s + 1}\gamma^{n_s + 1} \tag{13}$$

$$G_{sv}(\gamma, \chi) = \frac{H_{sv}}{n_{sv} + 1}(\gamma\chi)^{n_{sv} + 1} \tag{14}$$

with $H_g$ being a material parameter characterizing intergranular interactions and $n_g$ is a coefficient characterizing the interaction non linearity evolution. The coefficients $n_v$, $n_s$ and $n_{sv}$ reflect the nonlinearities of these interactions. The terms $H_v$, $H_s$ and $H_{sv}$ are, respectively, the interaction scalar coefficients between the martensite variants, the slip systems, and the martensite variants and the slip systems. In order to consider an equivalent macroscopic approach, the micromechanical formulation is simplified as given in Peultier et al. (2006) leading to scalar parameters for interactions. Therefore, only one scalar variable defines in a global way for each interaction. The state variables are subjected to the physical condition that the volume fraction of martensite can not be less than 0 or greater than 1, expressed by the inequality as:

$$0 \leq \chi \leq 1 \tag{15}$$

The introduction of Lagrange multipliers $\ell_1$ and $\ell_2$ allows to take into account for these physical constraints. They ensure Kuhn and Tucker conditions as given bellow:

$$\begin{cases} \ell_1 \geq 0 \ and \ \ell_1\chi = 0 \\ \ell_2 \geq 0 \ and \ \ell_2(1 - \chi) = 0 \end{cases} \tag{16}$$

A corresponding inner potential $\Psi_{IC}$ is defined as:

$$\psi_{IC} = -\ell_1\chi - \ell_2(1 - \chi) \tag{17}$$

A Lagrangian is then built as the sum of Helmholtz's free energy and the potential of inner conditions as:

$$\Im = \frac{\mu}{2}(I_{\mathbf{C}_{el}} - 3) - \mu \ln J + \frac{\lambda}{2}(\ln J)^2 + c_v\left[(T - T_0) - T \ln\left(\frac{T}{T_0}\right)\right] + B(T - T_0)\chi$$
$$+ G_g(\mathbf{E}_{ine}) + [G_v(\chi) + (1 - \chi)G_s(\gamma) + G_{sv}(\gamma, \chi)] - \ell_1\chi - \ell_2(1 - \chi) \tag{18}$$

### 3.2. Inelastic driving and yield forces

At this step, the second law of thermodynamics is taken into account. It asserts that the entropy production rate $\xi$ is always greater than or equal to the heating rate (heat flux vector $\mathbf{q}$ multiplied by the temperature gradient $\mathbf{grad}\ T$) divided by the temperature $T$. As a result, the Clausius-Duhem inequality takes the following form:

$$-(\dot{\Im} + \xi\dot{T}) + \mathbf{S} : \dot{\mathbf{E}} - \mathbf{q}\frac{\mathbf{grad}\ T}{T} \geq 0 \tag{19}$$

with $\mathbf{S}$ being the second Piola-Kirchhoff tensor. The temperature is assumed homogeneous on the RVE.

$$\mathbf{grad}\ T = 0 \tag{20}$$

Assuming that the Lagrangian $\Im$ is an isotropic function of $\mathbf{C}_{el}$, outcomes that $\mathbf{C}_{el}$ is coaxial with $\frac{\partial \Im}{\partial \mathbf{C}_{el}}$, this latter property achieves the symmetric property for $\frac{\partial \Im}{\partial \mathbf{C}_{el}}$ which can be expressed mathematically as follows:

$$\mathbf{C}_{el}\frac{\partial \Im}{\partial \mathbf{C}_{el}} = \frac{\partial \Im}{\partial \mathbf{C}_{el}}\mathbf{C}_{el} \tag{21}$$

Additive decomposition of strain rate for different finite strains inelastic processes was introduced in (Levitas, 1996). For a Fe-SMA, the symmetric inelastic strain rate is the sum of phase transformation and plastic slip strain rates (Feng and Levitas, 2017):

$$\mathbf{D}_{ine} = \mathbf{D}_{tr} + \mathbf{D}_{pl} \tag{22}$$

ARTICLE IN PRESS

A. Sallami, et al.                                                                                    International Journal of Plasticity xxx (xxxx) xxx–xxx

$$\mathbf{D}_{tr} = \dot{\chi}\, \bar{\varepsilon}_{\max}^{tr} \mathbf{N}^{tr} \tag{23}$$

$$\mathbf{D}_{pl} = (1 - \chi)\dot{\gamma}\mathbf{N}^{pl} \tag{24}$$

This last relation involves the term $(1 - \chi)$ which translates the assumption of plasticity development only in the austenite phase due to the very high yield stress for the activation of plasticity in martensite variants. Introducing the derived Lagrangian (18) and using (7) as well as equations (4), (5), (21), (23) and (24), equation (19) becomes:

$$
\begin{aligned}
&\left(\mathbf{S} - 2\mathbf{F}_{ine}^{-1}\frac{\partial \mathfrak{J}}{\partial \mathbf{C}_{el}}\mathbf{F}_{ine}^{-T}\right) : \frac{1}{2}\dot{\mathbf{C}} + \left(2\mathbf{C}_{el}\frac{\partial \mathfrak{J}}{\partial \mathbf{C}_{el}}\right) : (\dot{\chi}\,\bar{\varepsilon}_{\max}^{tr}\mathbf{N}^{tr} + (1 - \chi)\dot{\gamma}\mathbf{N}^{pl}) \\
&+ \left[\bar{\varepsilon}_{\max}^{tr}\mathbf{F}_{ine}\frac{\partial G_g(\mathbf{E}^{ine})}{\partial \mathbf{E}^{ine}}\mathbf{F}_{ine}^{T} : \mathbf{N}^{tr} - B(T - T_0) - \frac{\partial G_v}{\partial \chi} + G_s - \frac{\partial G_{sv}}{\partial \chi} + \ell_1 - \ell_2\right]\dot{\chi} \\
&+ \left[(1 - \chi)\left(\mathbf{F}_{ine}\frac{\partial G_g(\mathbf{E}^{ine})}{\partial \mathbf{E}^{ine}}\mathbf{F}_{ine}^{T} : \mathbf{N}^{pl} - \frac{\partial G_s}{\partial \gamma}\right) - \frac{\partial G_{sv}}{\partial \gamma}\right]\dot{\gamma} + \left[c_v \ln\left(\frac{T}{T_0}\right) - \chi B - \xi\right]\dot{T} \geq 0
\end{aligned} \tag{25}
$$

where $\mathbf{N}_{tr}$ and $\mathbf{N}_{pl}$ are the flow direction vectors, for phase transformation and plasticity respectively, obtained as follows (Khalil et al., 2012); (Cissé et al., 2017):

$$
\mathbf{N}_{tr} = \begin{cases} \frac{3}{2}\frac{\mathbf{S}^D}{S^{eq}} & \text{if } S^{eq} \neq 0 \\ \frac{\mathbf{E}_{tr}}{E_{tr}^{eq}} & \text{if } S^{eq} = 0 \end{cases} \quad ; \quad \mathbf{N}_{pl} = \begin{cases} \frac{3}{2}\frac{\mathbf{S}^D}{S^{eq}} & \text{if } S^{eq} \neq 0 \\ \frac{\mathbf{E}_{pl}}{E_{pl}^{eq}} & \text{if } S^{eq} = 0 \end{cases} \tag{26}
$$

where $\mathbf{S}^D$ denotes the second Piola-Kirchhoff stress deviator, $S^{eq}$ is the equivalent second Piola-Kirchhoff stress in the von Mises sense, and $E_\alpha^{eq}$ denotes the equivalent Green-Lagrange strain, with $\alpha = [tr, pl]$ :

$$\mathbf{S}^D = \mathbf{S} - \frac{1}{3}tr(\mathbf{S}) \tag{27}$$

$$S^{eq} = \sqrt{\frac{3}{2}\mathbf{S}^D : \mathbf{S}^D} \tag{28}$$

$$E_\alpha^{eq} = \sqrt{\frac{2}{3}\mathbf{E}_\alpha : \mathbf{E}_\alpha} \tag{29}$$

As the elastic behavior and the heating-cooling process are reversible and occur without dissipation, the second principle of thermodynamics leads to:

$$\mathbf{S} = 2\mathbf{F}_{ine}^{-1}\frac{\partial \mathfrak{J}}{\partial \mathbf{C}_{el}}\mathbf{F}_{ine}^{-T} \tag{30}$$

$$\xi = c_v \ln\left(\frac{T}{T_0}\right) - \chi B \tag{31}$$

The residual inequality leads to:

$$\Lambda_{dr}^{\chi}\dot{\chi} + \Lambda_{dr}^{\gamma}\dot{\gamma} \geq 0 \tag{32}$$

with $\Lambda_{dr}^{\chi}$ and $\Lambda_{dr}^{\gamma}$ being the phase transformation and the plastic thermodynamic driving forces, respectively, defined as:

$$
\begin{aligned}
\Lambda_{dr}^{\chi} = \bar{\varepsilon}_{\max}^{tr}(\mathbf{M} + H_g(\mathbf{E}_{ine} : \mathbf{E}_{ine})^{n_g}\mathbf{F}_{ine}\mathbf{E}_{ine}\mathbf{F}_{ine}^{T}) : \mathbf{N}^{tr} - B(T - T_0) - H_v\chi^{n_v} \\
+ \frac{H_s}{(n_s + 1)}\gamma^{n_s+1} - H_{sv}\gamma\left(\chi\gamma\right)^{n_{sv}} + \ell_1 - \ell_2
\end{aligned} \tag{33}
$$

$$
\begin{aligned}
\Lambda_{dr}^{\gamma} = (1 - \chi)(\mathbf{M} + H_g(\mathbf{E}_{ine} : \mathbf{E}_{ine})^{n_g}\mathbf{F}_{ine}\mathbf{E}_{ine}\mathbf{F}_{ine}^{T}) : \mathbf{N}^{pl} \\
- (1 - \chi)H_s\gamma^{n_s} - H_{sv}\chi(\chi\gamma)^{n_{sv}}
\end{aligned} \tag{34}
$$

whereas the symmetric Mandel Tensor $\mathbf{M}$ (The coaxiality of $\mathbf{C}_{el}$ and $\frac{\partial \mathfrak{J}}{\partial \mathbf{C}_{el}}$ involving the symmetry of $\mathbf{M}$) written as:

$$\mathbf{M} = 2\mathbf{C}_{el}\frac{\partial \mathfrak{J}}{\partial \mathbf{C}_{el}} \tag{35}$$

To ensure the positivity of the dissipation of plastic slip and phase transformation, either for forward or reverse phase transformation, indicated in (32), the ensuring evolution equations are built with respect to the accumulative plastic strain $\gamma$ and the volume fraction of martensite $\chi$, respectively, and are given as:

$$
\begin{aligned}
\dot{\gamma} &= \dot{\kappa}^{\gamma} \\
\dot{\chi} &= \dot{\kappa}^{\chi} Sgn(\Lambda_{dr}^{\chi})
\end{aligned} \tag{36}
$$

with $\dot{\kappa}^{\chi}$ and $\dot{\kappa}^{\gamma}$ being non negative-multipliers. The function $Sgn(.)$ is used to express the sign of $\Lambda_{dr}^{\chi}$. This function is exploited to

distinguish the forward and the reverse phase transformation.

The yield forces for forward phase transformation, reverse phase transformation, and plastic slip are defined, respectively, as follows:

$$\Lambda_y^{tr,m} = \sigma_y^m \bar{\varepsilon}_{tr}^{\max} + \zeta_m (T_0 - M_s) - H_\gamma \gamma^2 \tag{37}$$

$$\Lambda_y^{tr,a} = \sigma_y^a \bar{\varepsilon}_{tr}^{\max} + \zeta_a (T_0 - A_s) - H_\chi \chi \tag{38}$$

$$\Lambda_y^{pl} = \sigma_y^\gamma - K_T T \tag{39}$$

with $\zeta_a$ and $\zeta_m$ being control parameters (Cissé et al., 2017). $M_s$ is the start forward martensitic transformation temperature, $A_s$ is the start reverse martensitic transformation, $\sigma_y^m$, $\sigma_y^a$, and $\sigma_y^\gamma$ are, respectively, the yield stress of forward and reverse phase transformation and plasticity. $\bar{\varepsilon}_{tr}^{\max}$ is the equivalent maximal transformation strain for saturation (for $\chi = 1$) and $K_T$ represents the evolution of slope of the yield plastic stress with the temperature. The determination of the activated process needs the introduction of three loading surfaces: $\Upsilon_{tr}^m$ for forward transformation, $\Upsilon_{tr}^a$ for reverse transformation, and $\Upsilon_{pl}^a$ for plasticity. They correspond to the difference between driving and yield forces as follows:

$$\Upsilon_{tr}^m = \Lambda_{dr}^\chi - \Lambda_y^{tr,m} \tag{40}$$

$$\Upsilon_{tr}^a = -\Lambda_{dr}^\chi - \Lambda_y^{tr,a} \tag{41}$$

$$\Upsilon_{pl}^a = \Lambda_{dr}^\gamma - \Lambda_y^{pl} \tag{42}$$

These loading functions have to satisfy the Kuhn–Tucker conditions for forward and reverse phase transformation and plasticity:

$$\begin{cases} \Upsilon_{tr}^m \le 0, \quad \dot{\chi} \ge 0, \quad \dot{\chi}\Upsilon_{tr}^m = 0 \\ \Upsilon_{tr}^a \le 0, \quad -\dot{\chi} \ge 0, \quad -\dot{\chi}\Upsilon_{tr}^a = 0 \\ \Upsilon_{pl}^a \le 0, \quad \dot{\gamma} \ge 0, \quad \dot{\gamma}\Upsilon_{pl}^a = 0 \end{cases} \tag{43}$$

Therefore, Table 1 summarizes the constitutive equation system to be solved in order to predict the thermomechanical behavior for a given loading. The next section describes how this system is solved with an implicit integration scheme.

**Table 1**
Summary of the constitutive equations.

| Deformation gradients |
| --- |
| $\mathbf{F} = \mathbf{F}_{el}\mathbf{F}_{ine}$ |
| $\mathbf{F}_{ine} = \mathbf{F}_{tr}\mathbf{F}_{pl}$ |
| Strain quantities |
| $\mathbf{C} = \mathbf{F}^T\mathbf{F}$ |
| $\mathbf{C}_{ine} = \mathbf{F}_{ine}^T\mathbf{F}_{ine}$ |
| $\mathbf{E} = \frac{1}{2}(\mathbf{C} - \mathbf{I})$ |
| $\mathbf{E}_{ine} = \frac{1}{2}(\mathbf{C}_{ine} - \mathbf{I})$ |
| $\mathbf{H} = \frac{1}{2}\ln(\mathbf{C})$ |
| Stress quantities |
| $\mathbf{S} = \mu\mathbf{C}_{ine}^{-1} + (\lambda\ln(J) - \mu)\mathbf{C}^{-1}$ |
| $\mathbf{M} = \frac{\mu}{2}\mathbf{C}_{ine}^{-1}\mathbf{C}\mathbf{C}_{ine}^{-1} + \frac{1}{2}(\lambda\ln(J) - \mu)\mathbf{C}_{ine}^{-1}$ |
| $\sigma = \frac{1}{J}\mathbf{F}\mathbf{S}\mathbf{F}^T$ |
| Loading functions |
| $\Upsilon_{tr}^m = \Lambda_{dr}^\chi - \Lambda_y^{tr,m}$ |
| $\Upsilon_{tr}^a = -\Lambda_{dr}^\chi - \Lambda_y^{tr,a}$ |
| $\Upsilon_{pl}^a = \Lambda_{dr}^\gamma - \Lambda_y^{pl}$ |
| Kuhn-Tucker conditions on the loading functions |
| $\Upsilon_{tr}^m \le 0, \quad \dot{\chi} \ge 0, \quad \dot{\chi}\Upsilon_{tr}^m = 0$ |
| $\Upsilon_{tr}^a \le 0, \quad -\dot{\chi} \ge 0, \quad -\dot{\chi}\Upsilon_{tr}^a = 0$ |
| $\Upsilon_{pl}^a \le 0, \quad \dot{\gamma} \ge 0, \quad \dot{\gamma}\Upsilon_{pl}^a = 0$ |
| Kuhn-Tucker conditions on the state variables |
| $\ell_1 \ge 0, \quad \ell_1\chi = 0$ |
| $\ell_2 \ge 0, \quad \ell_2(1 - \chi) = 0$ |
| Flow rules |
| $\mathbf{D}_{ine} = \mathbf{D}_{tr} + \mathbf{D}_{pl}$ |
| $\mathbf{D}_{tr} = \dot{\chi}\bar{\varepsilon}_{\max}^{tr}\mathbf{N}^{tr}$ |
| $\mathbf{D}_{pl} = (1 - \chi)\dot{\gamma}\mathbf{N}^{pl}$ |

ARTICLE IN PRESS

A. Sallami, et al.                                                                                    International Journal of Plasticity xxx (xxxx) xxx–xxx

## 4. Constitutive equations: Resolution algorithm

The constitutive equations are solved with the Newton-Raphson method combined to the return mapping technique (elastic predictor-inelastic corrector procedure) using the Matlab software. An exponential integration scheme is adopted to update the inelastic deformation gradient.

$$\mathbf{F}_{ine}^{n+1} = \exp(\Delta\mathbf{D}_{ine}^{n+1})\mathbf{F}_{ine}^n \tag{44}$$

where $\Delta\mathbf{D} = \mathbf{D}\Delta t$. Reminding that for any invertible matrix $\mathbf{B}$, the tensor exponential satisfies $\exp(\mathbf{B})^{-1} = \exp(-\mathbf{B})$. Using this latter relation along with equations (1) and (44) leads to:

$$\mathbf{F}_{el}^{n+1} = \mathbf{F}_{el}^{trial}\exp(-\Delta\mathbf{D}_{ine}^{n+1}) \tag{45}$$

where $\mathbf{F}_{el}^{trial} = \Delta\mathbf{F}\mathbf{F}_{el}^n$, and $\Delta\mathbf{F}$ is an incremental deformation gradient, for a local perturbation. The incremental form of the global deformation gradient can be given as:

$$\mathbf{F}^{n+1} = \Delta\mathbf{F}\mathbf{F}_{el}^n\mathbf{F}_{tr}^n\mathbf{F}_{pl}^n\exp(-\Delta\mathbf{D}_{ine}^{n+1}) \tag{46}$$

The incremental form for the temperature evolution is defined as follows:

$$T^{n+1} = T^n + \Delta T \tag{47}$$

Using Matlab software, the first step defines the known initial states. In the second step, iterative scheme based on the return mapping procedure allows to identify which mechanisms are activated and to determine the increment for $\chi$ and $\gamma$ solutions of the system in Table 1. If the trial state is admissible, the step is elastic. Otherwise, the step is inelastic and internal variables for phase transformation and/or plasticity have to be updated. To solve the constitutive equations, time-discrete incremental equations are rewritten over a discrete time intervals $[t_n; t_{n+1}]$ where $n$ indicates the nth kinematic time instant. For the first increment, all these gradients of deformation are isochoric ($\mathbf{F}_{el}^0 = \mathbf{F}_{tr}^0 = \mathbf{F}_{pl}^0 = \mathbf{I}$) with $\mathbf{I}$ being the identity second order tensor. Also an initializing form for the volume fraction of martensite and the accumulative plastic strain to be zero ($\chi^0 = \gamma^0 = 0$), i.e., the Fe-SMA is purely austenitic and there are no initial or residual solicitations. Then, using the incremental form of the deformation gradient in equation (46) to quantify all model constitutive equations, an exponential mapping method updates the phase transformation and plastic gradient deformations as follows:

$$\mathbf{F}_{tr}^{n+1} = \exp(\Delta\mathbf{D}_{tr}^{n+1})\mathbf{F}_{tr}^n$$
$$\mathbf{F}_{pl}^{n+1} = \exp(\Delta\mathbf{D}_{pl}^{n+1})\mathbf{F}_{pl}^n \tag{48}$$

The computation of the total and the inelastic right Cauchy Green tensors, $\mathbf{C}$ and $\mathbf{C}_{ine}$, respectively, allows to determine the second Piola-Kirchhoff, $\mathbf{S}$, and Mandel, $\mathbf{M}$, stresses quantities which are used to calculate the different loading functions. Based on the loading functions values, the typical of behavior of the Fe-SMA (Elasticity, Forward Phase Transformation, Reverse Phase Transformation, Plastic Slip, coupling form between Forward Phase Transformation/Plastic Slip and coupling form between Reverse Phase Transformation/Plastic Slip) can be determined and it allows to quantify the evolution of the internal variables. An implicit integration scheme based on the Newton-Raphson method used to extract the internal variables multipliers. Since the internal variables multipliers are calculated, the evolution equation of the martensite volume fraction and the accumulative plastic strain can be rewritten using the backward Euler approximation as follows:

$$\chi^{n+1} = \chi^n + \Delta\kappa^\chi Sgn(\Lambda_{dr}^\chi) \tag{49}$$

$$\gamma^{n+1} = \gamma^n + \Delta\kappa^\gamma \tag{50}$$

with $\Delta\kappa^\chi = \dot{\kappa}^\chi\Delta t$ and $\Delta\kappa^\gamma = \dot{\kappa}^\gamma\Delta t$ are respectively the phase transformation and plasticity increments at time $t_{n+1}$. After the determination of the internal variables, they are inserted in the function which defines the strain rate for phase transformation and plasticity as:

$$\Delta\mathbf{D}_{tr}^{n+1} = \Delta\kappa^\chi\bar{\varepsilon}_{max}^{tr}\mathbf{N}_{tr}^n \tag{51}$$

$$\Delta\mathbf{D}_{pl}^{n+1} = (1 - \chi^{n+1})\Delta\kappa^\gamma\mathbf{N}_{pl}^n \tag{52}$$

Remembering that the total inelastic strain rate is the sum of the phase transformation and the plastic one as:

$$\Delta\mathbf{D}_{ine}^{n+1} = \Delta\mathbf{D}_{tr}^{n+1} + \Delta\mathbf{D}_{pl}^{n+1} \tag{53}$$

Introducing (53) into the equation defining the elastic predictor (45) allows to predict the next increment. The same procedure is repeated until reaching the desired level of strain. Fig. 3 illustrates the algorithm adopted to solve the finite strain problem in a given material point.

## 5. Results and discussion

In order to verify the developed model, small and finite strain simulations are carried out and compared with the experimental data of Khalil et al. (2013) and the numerical results of Khalil et al. (2012) at different tension loading levels followed by a heating-
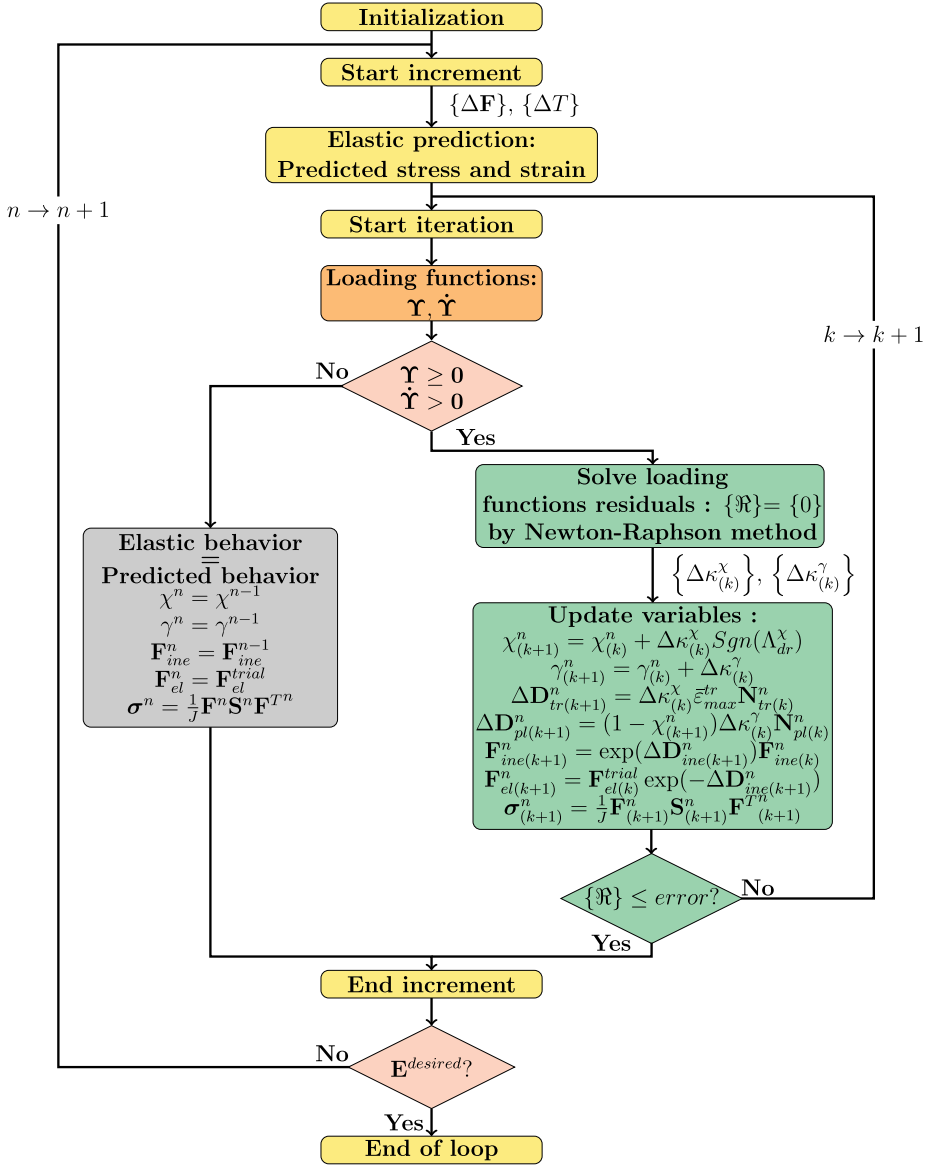
**Fig. 3.** Solution algorithm.

cooling process. Then, finite strain uni-axial simulations for higher strain level are carried out to predict the corresponding Fe-SMA behavior. In the case of a uni-axial tension test, $\Delta \mathbf{F}$ is defined as:

$$\Delta \mathbf{F} = \begin{bmatrix} \varrho & 0 & 0 \\ 0 & \frac{1}{\sqrt{\varrho}} & 0 \\ 0 & 0 & \frac{1}{\sqrt{\varrho}} \end{bmatrix}; \quad \varrho = 1 + \frac{\Delta u_1}{\Delta X_1} = 1 + 10^{-6}$$

(54)

The material parameters considered for small strain simulations are gathered in Table 2. They were identified starting from experimental results in Khalil et al. (2013).

## 5.1. Small strain model response

This section deals with a series of uni-axial loadings described by Fig. 4 with small strain level (tension loading-unloading followed by a heating-cooling). Numerical results are compared to the experimental data of Khalil et al. (2013) for the Fe-Mn$_{31.6}$-Si$_{6.45}$-C$_{0.018}$(wt%). Table 2 illustrates the model parameters. Three different temperatures (20, 50 and 130°C) were considered for the uni-axial applied loading. Each temperature corresponds to special behavior of the Fe-SMA (20°C: Only phase transformation; 130°C:

**Table 2**
Model parameters for Fe–Mn$_{31.6}$-Si$_{6.45}$-C$_{0.018}$(wt%).

| Parameter | Value | Parameter | Value |
|---|---|---|---|
| $\sigma_y^m$ (MPa) | 137.7 | $A_s$ (°C) | 96 |
| $\sigma_y^a$ (MPa) | 125.2 | $T_0$ (°C) | 79.4 |
| $\sigma_y^\gamma$ (MPa) | 210 | $H_v$ (MPa) | 27.2 |
| $\nu$ | 0.3 | $H_s$ (MPa) | 632.5 |
| $\mu$ (MPa) | 65385 | $H_{sv}$ (MPa) | 1000 |
| $\lambda$ (MPa) | 98077 | $H_g$ (MPa) | 627 |
| $\bar{\varepsilon}_{max}^{tr}$ | 0.048 | $n_v$ | 0.44 |
| $\zeta_m$ (MPa/°C) | 0.086 | $n_s$ | 0.55 |
| $\zeta_a$ (MPa/°C) | 0.036 | $n_{sv}$ | 0.45 |
| $B$ (MPa/°C) | 0.104 | $n_g$ | 3.07 |
| $K_T$ (MPa/°C) | 0.45 | $H_\gamma$ (MPa) | 500 |
| $M_s$ (°C) | −25 | $H_\chi$ (MPa) | −3 |
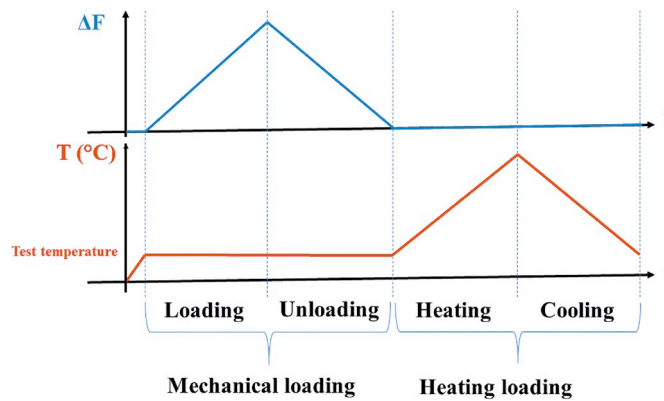


**Fig. 4.** Thermomechanical loading.

Only plasticity; 50°C: Coupling between phase transformation and plasticity). The applied thermomechanical loading cycle consists of a mechanical loading/unloading followed by heating to activate the reverse transformation (Fig. 4). The heating allows to quantify the part of strain due to the phase transformation compared to that due to the plasticity. Therefore, all the martensite created during the mechanical loading can be recovered by heating and the plastic strain remains permanent.
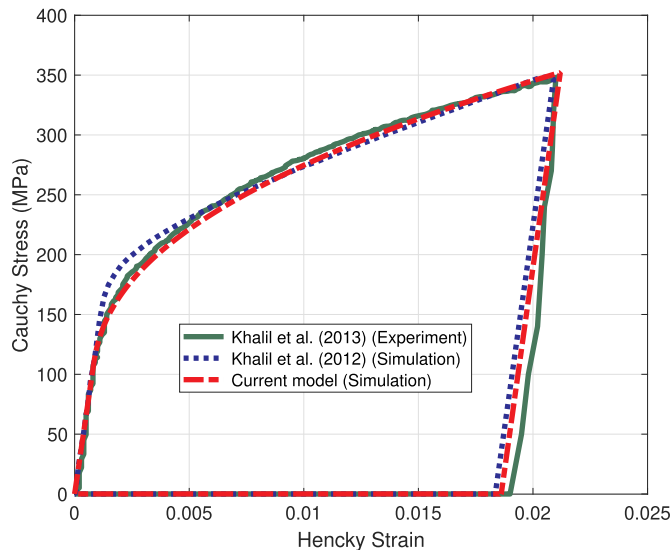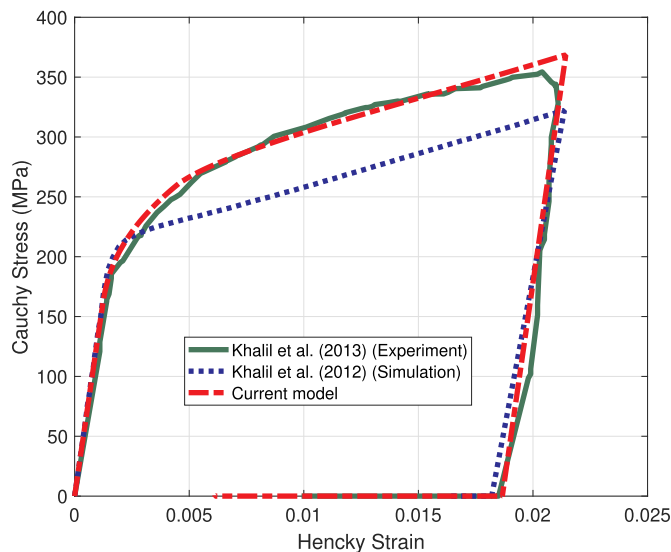


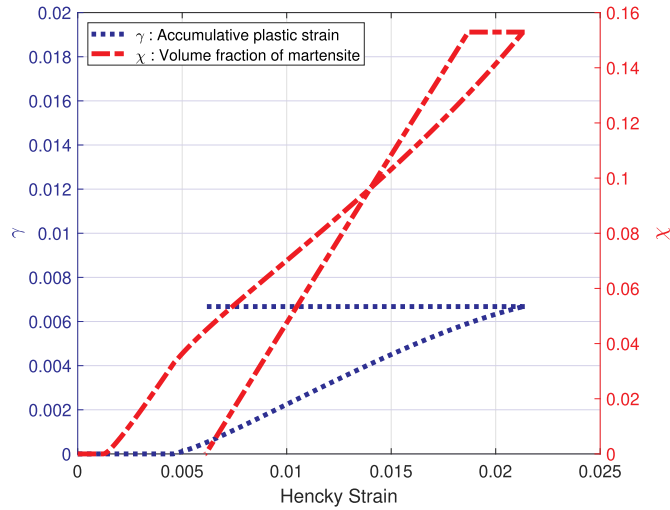**Fig. 5.** Experimental and simulated stress-strain behavior at 20° C.
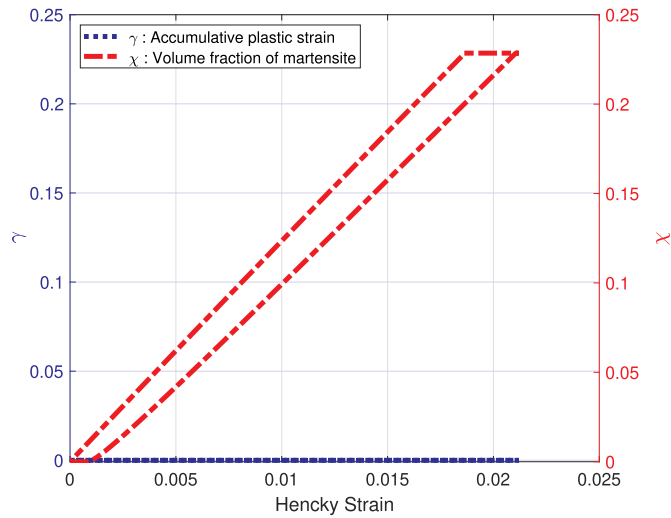
**Fig. 6.** Evolution of the volume fraction of martensite and the accumulative plastic strain function of strain at 20˚ C.

Fig. 5 depicts the comparison of present results with those of available experimental, and numerical data of (Khalil et al., 2012, 2013) based on small strain. The obtained results here show that the finite-strain model is in a good agreement with experimental data. For the level of 2.2% of strain at 20°C only phase transformation is activated. As shown in Fig. 6 the accumulative plastic strain remains stagnant and only the volume fraction of martensite increases during mechanical loading and decreases during heating, leading to the full strain recovery.

Fig. 7 shows a comparison between numerical and experimental results at 50°C for a uni-axial tensile test. The numerical curve is consistent with the experimental one. The present model describes Fe-SMA hardening compared to that of Khalil et al. (2012). At this temperature, Fe-SMA behavior exhibits a coupling between phase transformation and plasticity. After a heating cycle, a part of strain is recovered due to the reverse phase transformation and the other part is irreversible due to the plasticity of austenite. Fig. 8 shows the evolution of the volume fraction of martensite and the accumulative plastic strain as a function of strain during mechanical loading at 50°C. At first, only the transformation is activated (only the volume fraction of martensite evolves). Starting from a certain loading level, plasticity is occurred and the two mechanisms are active simultaneously. The martensite evolution slope is changed after the start of the plasticity, marking the fact that the activation of the plasticity hinders the development of the phase transformation. For this temperature, the inelastic strain corresponds to the two combined mechanisms, the phase transformation and the plastic slip.

Moreover, the comparison between the numerical and experimental results in Fig. 9 shows that the model is consistent with the experimental results at 130°C. Similarly, the present model describes the non-linear hardening more accurately than those of Khalil



**Fig. 7.** Experimental and simulated stress-strain behavior at 50˚ C.

A. Sallami, et al.

**Fig. 8.** Evolution of the volume fraction of martensite and the accumulative plastic strain function of strain at 50° C.
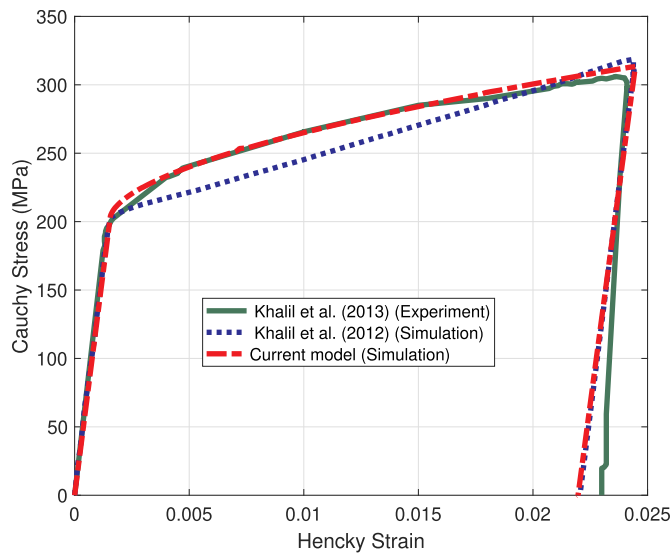


**Fig. 9.** Experimental and simulated stress-strain behavior at 130°C.

et al. (2012). Even after a heating cycle, the Fe-SMA maintains the same deformed configuration. Next, the study is focused on the evolution of the volume fraction of martensite and the accumulative plastic strain. Fig. 10 shows only the presence of plasticity and the strain is irreversible denoting the behavior is purely plastic.

Fig. 11 presents the 3D stress-strain-temperature diagram for the applied tensile loading at three constant temperatures. This diagram shows that the Fe-SMA behavior is affected by the sample's temperature. By going further from the $M_s$ temperature, the plastic behavior becomes dominant. Fig. 12 shows the corresponding curves in the temperature-strain diagram. It is given that, after a loading-unloading cycle, the elastic strain is recovered for each temperature. After heating, the strain is fully recovered at 20°C and only partially recovered at 50°C. This behavior brings out that the inelastic strain has a reversible part induced by phase transformation and a remnant part induced by plasticity. At 130°C temperature, the Fe-SMA behavior is purely plastic with a very low recovered strain during heating. It appears that the present model predicts well the Fe-SMA behavior for small strains. The next subsection presents the predicted Fe-SMA behavior for higher strain levels.

## 5.2. Results for uni-axial tensile tests with higher strain levels

The Fe-SMAs can reach high level strains due to their ductility. Hence, destructive quasi-static tensile tests for Fe-SMA type Fe-$Mn_{30}$–$Si_6$–$Cr_5$(wt%) is performed on a Dynamic Mechanical Analysis (DMA) machine type LTM1 Zwick/Roell at 3 different temperatures (20, 50 and 130°C). The capacity of the machine is ± 1 KN on loading and a temperature range of −80 to +250°C. The
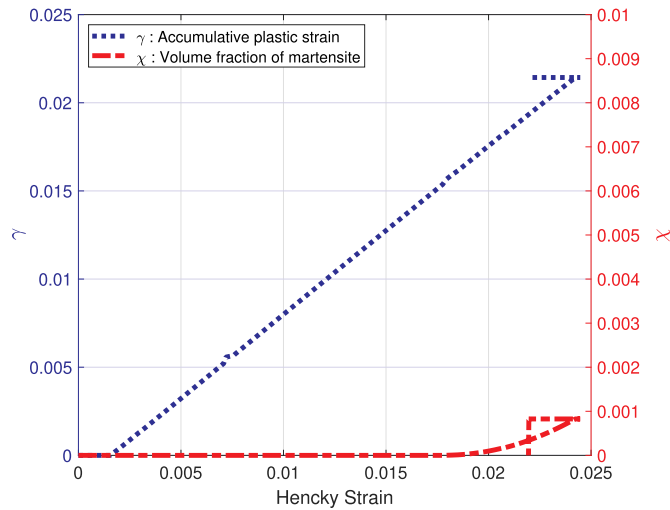
**Fig. 10.** Evolution of the volume fraction of martensite and the accumulative plastic strain function of strain at 130˚C.
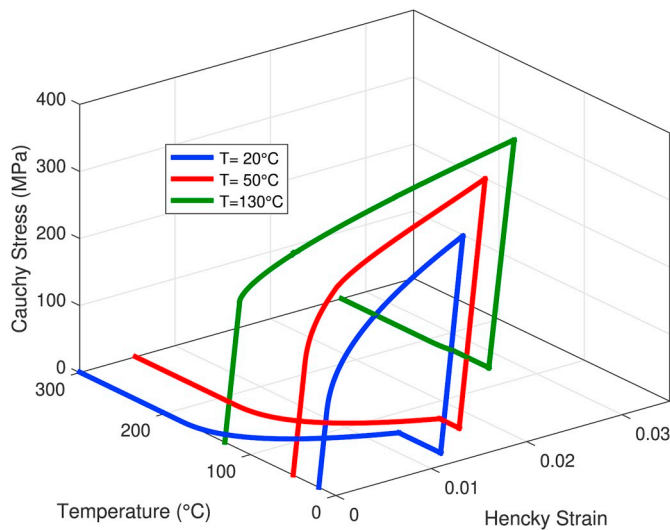


**Fig. 11.** Small strain 3D stress-strain-temperature diagram.

specimen used here has the following dimensions (35 mm × 1.25 mm × 1 mm). The model is adjusted with the obtained curves (Fig. 13). Table 3 shows the material corresponding new parameters of the Fe–-Mn$_{30}$–Si$_6$-Cr$_5$(wt%).

Simulations are carried out to predict Fe-SMA behavior for different temperature under uni-axial tensile tests at large strain. Fig. 14 highlights a simulation tensile test for 15, 20 and 25% of strain at 20, 50 and 130˚C, respectively. After a loading-unloading-heating cycle, a part of strain is recovered due to the reverse phase transformation.

Looking at the evolution of the internal variables in Fig. 15, the activation of the plasticity initially reduced the slope of the volume fraction of martensite. Then, the stable trend started when reaching 52% of the martensite. This is due to the trapped martensite variants (unlike the classical SMA which can be totally transformed). At this level, the accumulative plastic strain slope increased until reaching the desired strain.

For the 50˚C temperature, only 27% of martensite is created(Fig. 16), which decreases the recovered strain (Fig. 14).

At the 130˚C temperature, the accumulative plastic strain is activated initially (Fig. 17), and then, the martensite appears in consistency with the experimental observations on the temperature dependence of yield stresses outlined in the work of Bouraoui et al. (2008). This created martensite is in the order of 6.6%, which recovers a small part of the strain (Fig. 14).

For the Fe-SMA, increasing the strain activates the plasticity and prevents the phase transformation activation. This is the reason, in Figs. 18 and 19, the phase transformation strain quantities even in the 20˚C test are very small compared to the plastic strain.
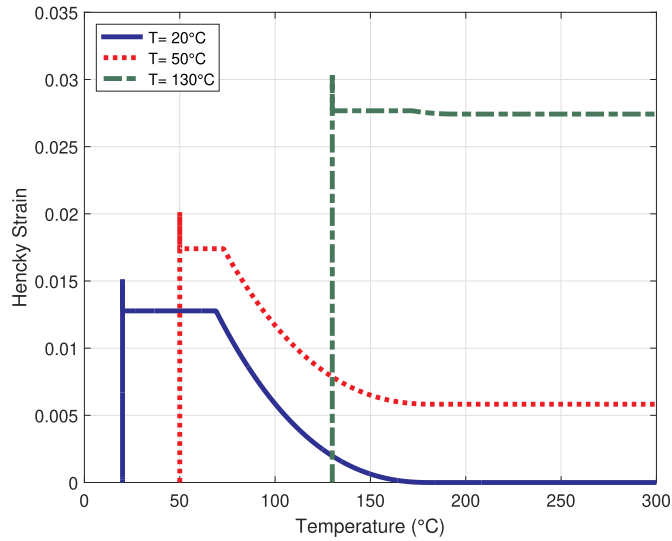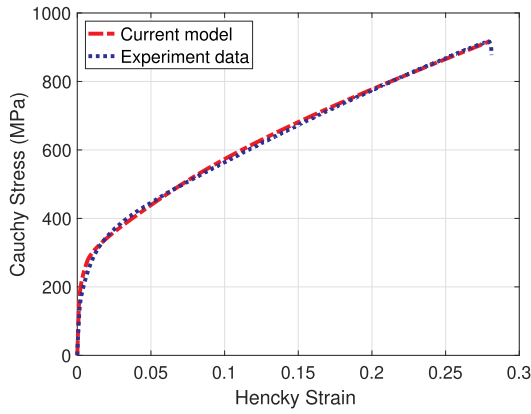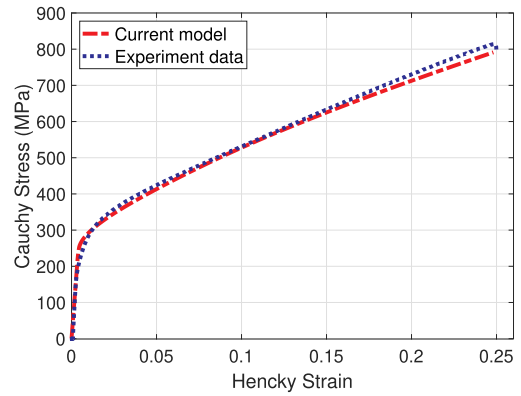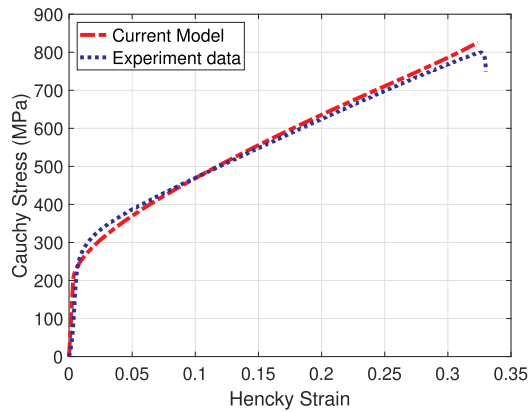
**Fig. 12.** Shape memory effect of an Fe-SMA response in small strain.



(a) T=20°C



(b) T=50°C



(c) T=130°C

**Fig. 13.** Experimental and simulated stress strain behavior at: (a) 20˚C, (b) 50˚C and (c) 130˚C.

**Table 3**
Model parameters of Fe–Mn$_{30}$–Si$_6$–Cr$_5$(wt%).

| Parameter | Value | Parameter | Value |
|---|---|---|---|
| $\sigma_y^m$ (MPa) | 117.7 | $A_s$ (°C) | 96 |
| $\sigma_y^a$ (MPa) | 100.2 | $T_0$ (°C) | 79.4 |
| $\sigma_y^\gamma$ (MPa) | 210 | $H_v$ (MPa) | 30.7 |
| $\nu$ | 0.3 | $H_s$ (MPa) | 632.5 |
| $\mu$ (MPa) | 46154 | $H_{sv}$ (MPa) | 2000 |
| $\lambda$ (MPa) | 69231 | $H_g$ (MPa) | 1254 |
| $\bar{\varepsilon}_{max}^{tr}$ | 0.05 | $n_v$ | 0.45 |
| $\zeta_m$ (MPa/°C) | 0.086 | $n_s$ | 0.55 |
| $\zeta_a$ (MPa/°C) | 0.036 | $n_{sv}$ | 0.45 |
| $B$ (MPa/°C) | 0.104 | $n_g$ | 3.07 |
| $K_T$ (MPa/°C) | 0.45 | $H_\gamma$ (MPa) | 500 |
| $M_s$ (°C) | −25 | $H_\chi$ (MPa) | −9 |
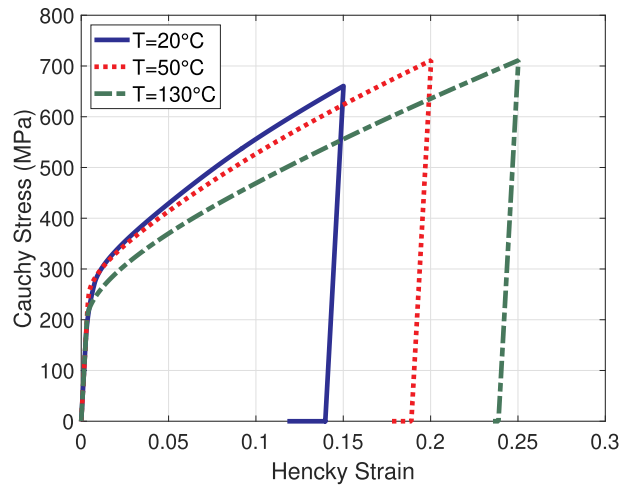


**Fig. 14.** Finite strain current model response at different temperatures.
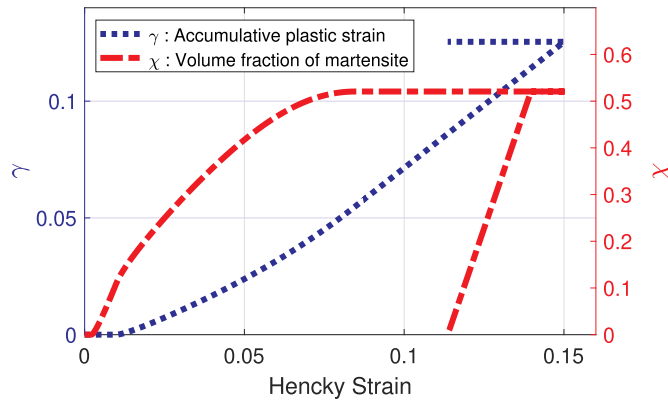


**Fig. 15.** Evolution of the volume fraction of martensite and the accumulative plastic strain function of strain at 20°C.

## 5.3. Results for multi-axial loadings with higher strain levels

In order to show the validity of the proposed model in the case of multi-axial loadings, an investigation of its prediction range under different complex loading paths (tensile-shear and bi-axial tensile tests) has been carried out within the large strain framework. The increment of the deformation gradient in the case of tensile-shear test has been defined as follows:

A. Sallami, et al.
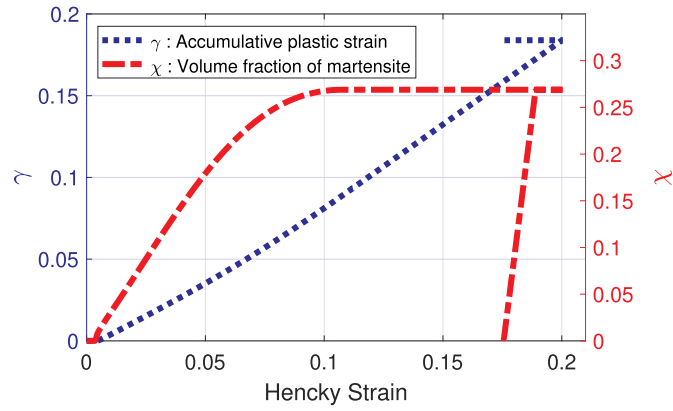
**Fig. 16.** Evolution of the volume fraction of martensite and the accumulative plastic strain function of strain at 50°C.
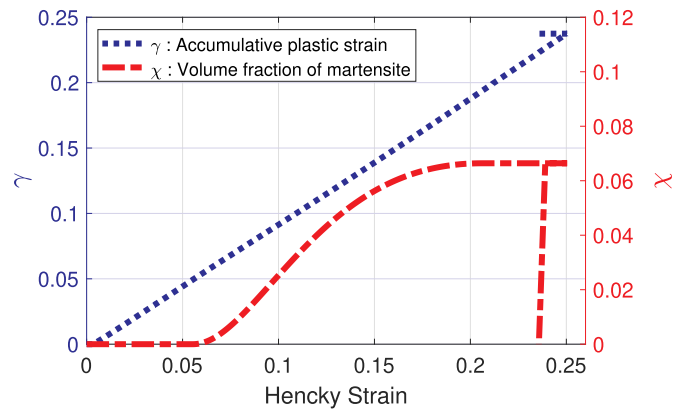


**Fig. 17.** Evolution of the volume fraction of martensite and the accumulative plastic strain function of strain at 130°C.
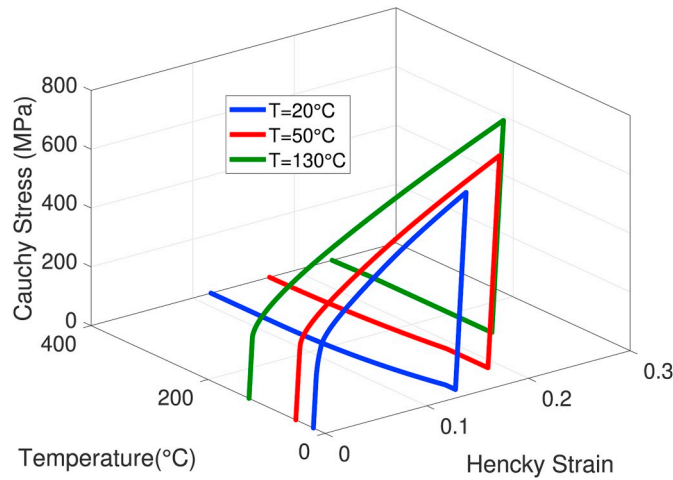


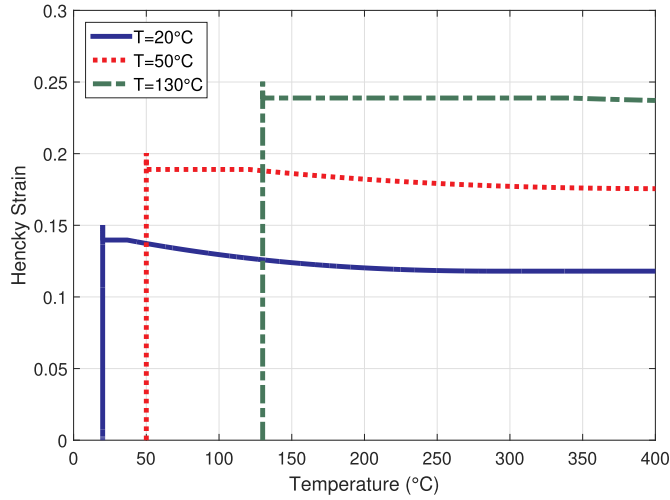**Fig. 18.** Finite strain 3D stress-strain-temperature diagram.

**Fig. 19.** Shape memory effect of an Fe-SMA response in finite strain.

$$\Delta \mathbf{F} = \begin{bmatrix} \varrho & \pi & 0 \\ 0 & \frac{1}{\sqrt{\varrho}} & 0 \\ 0 & 0 & \frac{1}{\sqrt{\varrho}} \end{bmatrix}$$

(55)

Two different values of the ratio between tension and shear strains have been defined ($\theta = \frac{H_{12}}{H_{11}}$ is equal to 0.5 or 0.9). Fig. 20 presents the 3D stress-strain-temperature diagram for the applied tensile-shear loading at three constant temperatures and under two different loading cases. The obtained results show that by increasing the ratio θ, the shear effect on the global behavior becomes more pronounced. At 20˚ C (Fig. 20a and b), the normal stress level inducing the transformation or plasticity is lower then the one for pure tension. Indeed, the shear stress component significantly contribute on the driving forces for phase transformation and plasticity. More then that, the ratio ($\theta = \frac{H_{12}}{H_{11}}$) modifies the recovered normal strain component. For the first ratio ($\theta_1 = 0.5$) after heating cycle the recovered normal strain is about 3.4% whereas the second ratio ($\theta_2 = 0.9$) leads to only 2.65% of recovered normal strain. Furthermore, for the second ratio ($\theta_2 = 0.9$), the maximum reached normal stress decreases compared to the loading with the first ratio ($\theta_1 = 0.5$). To remind, this value (the normal stress) is much higher in the case of pure tension. At 50˚ C (Fig. 20c and d), the same effect has been observed. At this temperature and like uni-axial tests, the recovered strain decreases. Additionally, shear loading has an influence on the recovered strain which decreases from 1.64% in the first ratio ($\theta_1 = 0.5$) to 1.31% in the second ratio ($\theta_2 = 0.9$). At 130˚ C (Fig. 20e and f), for both ratios ($\theta_1$ and $\theta_2$) the transformation strain remains negligible compared to plastic strain. As already seen for other temperatures, the normal stress decreases by increasing the ratio value.

Another complex loading path is investigated. It corresponds to a bi-axial tensile loading with a strain ratio ($\theta_3 = \frac{H_{22}}{H_{11}} = 0.8$) and at different constant temperatures. The increment of the corresponding deformation gradient has the following expression:

$$\Delta \mathbf{F} = \begin{bmatrix} \varrho_1 & 0 & 0 \\ 0 & \varrho_2 & 0 \\ 0 & 0 & \frac{1}{\varrho_1 \varrho_2} \end{bmatrix}$$

(56)

Fig. 21 presents the 3D stress-strain-temperature diagram. The combined bi-axial test has an influence on the yield stress for phase transformation and plasticity because of changes on the equivalent stress. Fig. 21a presents the 20˚ C bi-axial test. At this temperature, 3.17% of normal strain has been recovered due to the phase transformation compared to 3.92% of strain recovered in the case of pure tension. Furthermore, the maximum reached normal stress decreases compared to the pure tension. Also, at 50˚ C (Fig. 21b) the recovered normal strain and the maximum reached stress decrease comparing to pure tension test. At 130˚ C (Fig. 21c), the plasticity dominates the Fe-SMA behavior. Similar to the previous temperatures, in the bi-axial case the maximum reached normal stress decreases compared to pure tension one.

All the presented results show the capability of the proposed model to predict simple and complex loading paths at large strain levels.

## 6. Conclusions and prospects

In this paper, a constitutive finite-strain model for Iron-based SMAs (Fe-SMAs) is developed by generalizing the small-strain model. The finite-strain model is formed based on a multiplicative decomposition of the deformation gradient into elastic and inelastic elements. Furthermore, the inelastic deformation gradient is consists of elements of phase transformation and plasticity. The
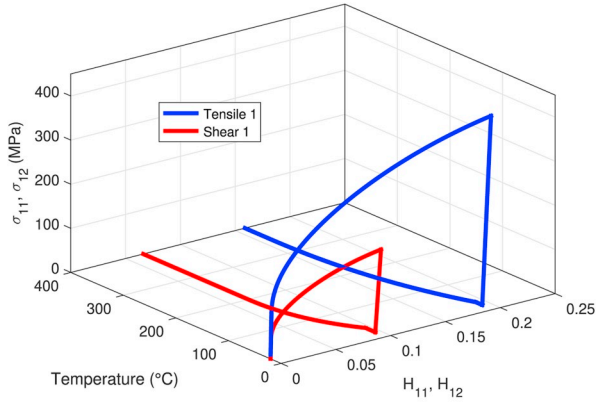
(a) T=20°C, $\theta_1$=0.5
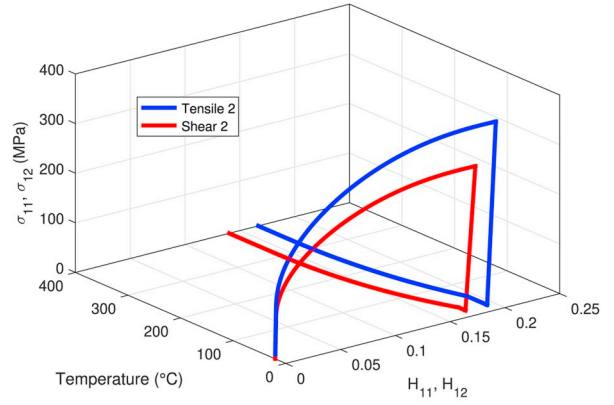
(b) T=20°C, $\theta_2$=0.9
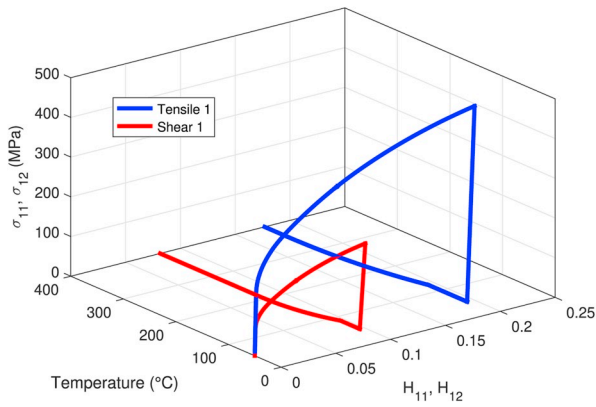
(c) T=50°C, $\theta_1$=0.5
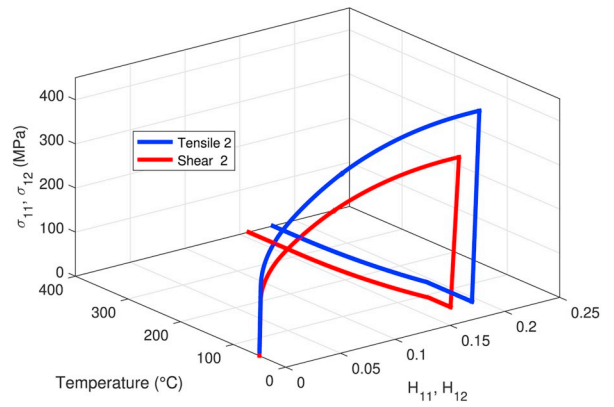
(d) T=50°C, $\theta_2$=0.9
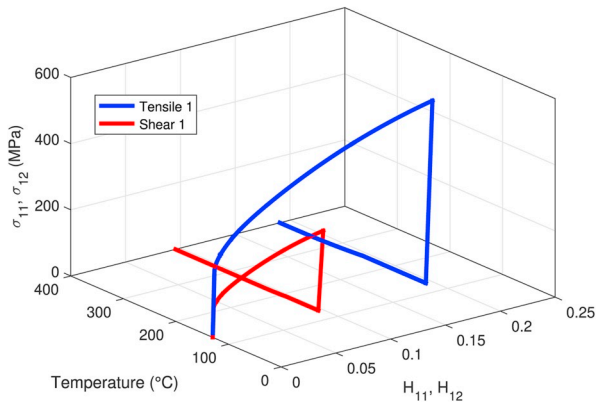
(e) T=130°C, $\theta_1$=0.5
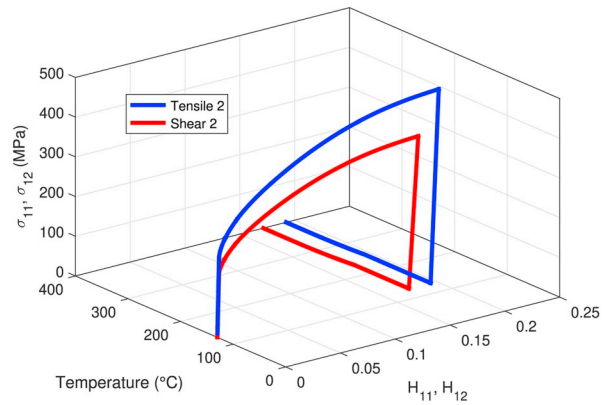
(f) T=130°C, $\theta_2$=0.9

**Fig. 20.** Combined tensile-shear test at different temperature and loading levels: (a-b) 20˚C, (c-d) 50˚C and (e-f) 130˚C.

constitutive equations are derived in a thermodynamically consistent framework involving Clausius-Duhem inequality. The constructed Lagrangien is a combination of a hyper-elastic and an inelastic energies that represent the part of the free energy of Helmholtz. The other part is a corresponding inner potential to introduce the conditions for, the martensite volume fraction. The coupling between the phase transformation and the plastic slip represents the distinguished behavior of the Fe-SMAs. In this model, two internal variables have been defined; the volume fraction of martensite $\chi$ and the accumulative plastic strain $\gamma$. These variables
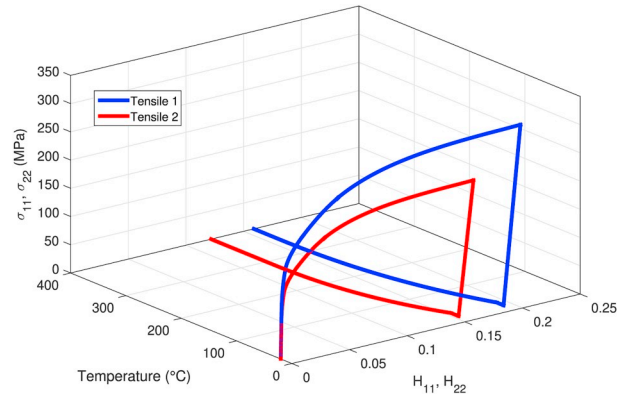
(a) T=20°C, $\theta_3$=0.8
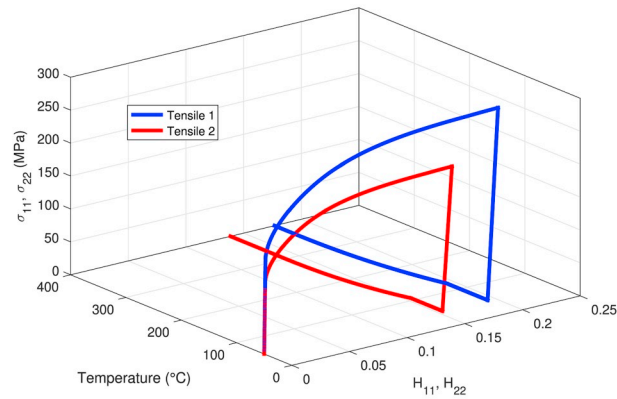


(b) T=50°C, $\theta_3$=0.8
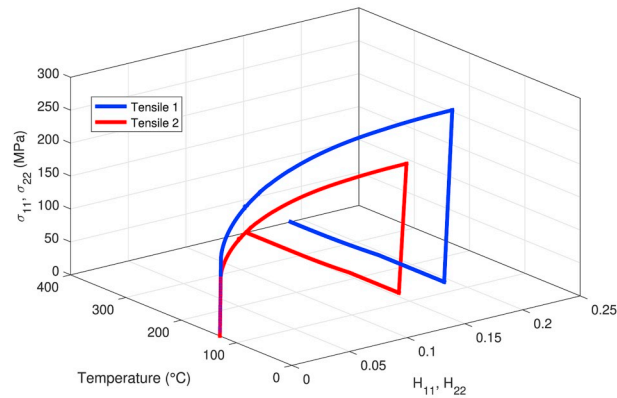


(c) T=130°C, $\theta_3$=0.8

**Fig. 21.** Bi-axial tensile test: (a) 20°C (b) 50°C and (c) 130°C.

are related to the different gradients of deformation. Furthermore, an exponential scheme is used to update the deformation gradients, and it is adopted to circumvent the singularity problems of the linear method.

An implicit integration scheme based on the Newton-Raphson method is applied to quantify the martensite volume fraction and the plastic slip by adopting an elastic predictor-inelastic corrector method for handling the corresponding stress-strain values. After calibration, the algorithm predicts the internal variable increments with respect to discrete-time. The obtained results either in small or finite strain simulations fulfill the fact that the internal variables evolve in accordance with the activated behavior. This new model

is in good agreement with experimental data. Also, different temperatures simulations are made for higher strain levels to predict an Fe-SMA response.

As perspective, this model will be implemented in the finite element code Abaqus via the subroutine UMAT in order to predict the response of an Iron-based SMA with complex geometry and/or under complex loading paths at large strains. Also, large displacements and rotations applications can be simulated with this model in order to check its capacity. Taking the mechanical forming simulation such us (lamination, stamping,) can be conducted by advantages of this model by comparing it with those developed in small strains. Since the present work does not take into account of the latent heat, as a future work, it will be addressed to model the effect of loading rates on the structure response. Also, the non-Schmid average effect at the macroscopic scale can be integrated in the future work by: (i) replacing the scalar interaction parameters by a tensorial ones leading to an anisotropic interactions and hardening, (ii) introducing a transformation saturation function taking into account the difference between tension and compression. Finally, larger strain experimental basis data will be required to verify the predicted behavior model response.

## References

Alkan, S., Ojha, A., Sehitoglu, H., 2018. The complexity of non-Schmid behavior in the CuZnAl shape memory alloy. J. Mech. Phys. Solids 114, 238–257. https://doi.org/10.1016/j.jmps.2018.02.017.

Alkan, S., Sehitoglu, H., 2017. Dislocation core effects on slip response of NiTi- a key to understanding shape memory. Int. J. Plast. 97, 126–144. https://doi.org/10.1016/j.ijplas.2017.05.012.

Alkan, S., Sehitoglu, H., 2019. Prediction of transformation stresses in NiTi shape memory alloy. Acta Mater. 175, 182–195. https://doi.org/10.1016/j.actamat.2019.06.009.

Arghavani, J., Auricchio, F., Naghdabadi, R., 2011. A finite strain kinematic hardening constitutive model based on hencky strain: general framework, solution algorithm and application to shape memory alloys. Int. J. Plast. 27, 940–961. https://doi.org/10.1016/j.ijplas.2010.10.006.

Bouraoui, T., Jemal, F., Ben Zineb, T., 2008. Tensile properties of a Fe-32Mn-6Si shape memory alloy. Strength Mater. 40, 203–211. https://doi.org/10.1007/s11223-008-9012-4.

Cao, B., Iwamoto, T., 2019. An experimental investigation on rate dependency of thermomechanical and stress-induced martensitic transformation behavior in Fe-28Mn-6Si-5Cr shape memory alloy under compression. Int. J. Impact Eng. 132, 103284. https://doi.org/10.1016/j.ijimpeng.2019.04.026.

Christ, D., Reese, S., 2009. A finite element model for shape memory alloys considering thermomechanical couplings at large strains. Int. J. Solids Struct. 46, 3694–3709. https://doi.org/10.1016/j.ijsolstr.2009.06.017.

Cissé, C., Zaki, W., Ben Zineb, T., 2016a. A review of constitutive models and modeling techniques for shape memory alloys. Int. J. Plast. 76, 244–284. https://doi.org/10.1016/j.ijplas.2015.08.006.

Cissé, C., Zaki, W., Ben Zineb, T., 2016b. A review of modeling techniques for advanced effects in shape memory alloy behavior. Smart Mater. Struct. 25, 1–36. https://doi.org/10.1088/0964-1726/25/10/103001.

Cissé, C., Zaki, W., Gu, X., Ben Zineb, T., 2017. A nonlinear 3D model for iron-based shape memory alloys considering different thermomechanical properties for austenite and martensite and coupling between transformation and plasticity. Mech. Mater. 107, 1–21. https://doi.org/10.1016/j.mechmat.2017.01.008.

Evangelista, V., Marfia, S., Sacco, E., 2009. A 3D SMA constitutive model in the framework of finite strain. Int. J. Numer. Methods Eng. 81, 761–785. https://doi.org/10.1002/nme.2717.

Feng, B., Levitas, V.I., 2017. Coupled elastoplasticity and plastic strain-induced phase transformation under high pressure and large strains: formulation and application to bn sample compressed in a diamond anvil cell. Int. J. Plast. 96, 156–181. https://doi.org/10.1016/j.ijplas.2017.05.002.

Fischer, F., Reisner, G., Werner, E., Tanaka, K., Cailletaud, G., Antretter, T., 2000. A new view on transformation induced plasticity (TRIP). Int. J. Plast. 16, 723–748. https://doi.org/10.1016/S0749-6419(99)00078-9.

Goliboroda, I., Rusinko, K., Tanaka, K., 1999. Description of an Fe-based shape memory alloy thermomechanical behavior in terms of the synthetic model. Comput. Mater. Sci. 13, 218–226. https://doi.org/10.1016/S0927-0256(98)00092-5.

Grilo, T.J., Vladimirov, I.N., Valente, R.A.F., Reese, S., 2016. A finite strain constitutive model for non-quadratic yield criteria and nonlinear kinematic/isotropic hardening: application to sheet metal forming. Arch. Appl. Mech. 86, 147–163. https://doi.org/10.1007/s00419-016-1117-9.

Hallberg, H., Håkansson, P., Ristinmaa, M., 2007. A constitutive model for the formation of martensite in austenitic steels under large strain plasticity. Int. J. Plast. 23, 1213–1239. https://doi.org/10.1016/j.ijplas.2006.11.002.

Jella, V., Ippili, S., Eom, J.H., Pammi, S., Jung, J.S., Tran, V.D., Nguyen, V.H., Kirakosyan, A., Yun, S., Kim, D., Sihn, M.R., Choi, J., Kim, Y.J., Kim, H.J., Yoon, S.G., 2019. A comprehensive review of flexible piezoelectric generators based on organic-inorganic metal halide perovskites. Nano Energy 57, 74–93. https://doi.org/10.1016/j.nanoen.2018.12.038.

Jemal, F., Bouraoui, T., Ben Zineb, T., Patoor, E., Bradaï, C., 2009. Modelling of martensitic transformation and plastic slip effects on the thermo-mechanical behaviour of Fe-based shape memory alloys. Mech. Mater. 41, 849–856. https://doi.org/10.1016/j.mechmat.2008.11.007.

Kalsar, R., Suwas, S., 2017. Deformation mechanisms during large strain deformation of high Mn TWIP steel. Mater. Sci. Eng. 700, 209–219. https://doi.org/10.1016/j.msea.2017.05.039.

Khalil, W., Mikolajczak, A., Bouby, C., Ben Zineb, T., 2012. A constitutive model for Fe-based shape memory alloy considering martensitic transformation and plastic sliding coupling: application to a finite element structural analysis. J. Intell. Mater. Syst. Struct. 23, 1143–1160. https://doi.org/10.1177/1045389X12442014.

Khalil, W., Saint-Sulpice, L., Chirani, S.A., Bouby, C., Mikolajczak, A., Ben Zineb, T., 2013. Experimental analysis of Fe-based shape memory alloy behavior under thermomechanical cyclic loading. Mech. Mater. 63, 1–11. https://doi.org/10.1016/j.mechmat.2013.04.002.

Kim, Y.Y., Kwon, Y.E., 2015. Review of magnetostrictive patch transducers and applications in ultrasonic nondestructive testing of waveguides. Ultrasonics 62, 3–19. https://doi.org/10.1016/j.ultras.2015.05.015.

Kokorin, V., Gunko, L., Shevchenko, O., 1993. Martensitic $\gamma \leftrightarrows \epsilon$ transformation in ausaged Fe-Co based alloys. Scr. Metall. Mater. 28, 35–40. https://doi.org/10.1016/0956-716X(93)90533-X.

Koval, Y.N., Kokorin, V.V., Khandros, L.G., 1979. Shape memory effect in Fe-NiCo-Ti alloys. Phys. Met. Metallogr. 48, 162–164.

Lee, E.H., 1969. Elastic-plastic deformation at finite strains. J. Appl. Mech. 36, 1–6. https://doi.org/10.1115/1.3564580.

Levitas, V.I., 1996. Large Deformation of Materials with Complex Rheological Properties at Normal and High Pressure. Nova Science Publishers, New York.

Levitas, V.I., 1998. Thermomechanical theory of martensitic phase transformations in inelastic materials. Int. J. Solids Struct. 35, 889–940. https://doi.org/10.1016/S0020-7683(97)00089-9.

Lin, H.C., Lin, K.M., 1996. An investigation of martensitic transformation in an Fe-30Mn-6Si shape memory alloy. Scr. Mater. 34, 343–347. https://doi.org/10.1016/S0956-716X(95)00549-B.

Lion, A., 2000. Constitutive modelling in finite thermoviscoplasticity: a physical approach based on nonlinear rheological models. Int. J. Plast. 16, 469–494. https://doi.org/10.1016/S0749-6419(99)00038-8.

Lookman, T., Balachandran, P.V., Xue, D., Hogden, J., Theiler, J., 2017. Statistical inference and adaptive design for materials discovery. Curr. Opin. Solid State Mater. Sci. 21, 121–128. https://doi.org/10.1016/j.cossms.2016.10.002.

Mahnken, R., Wolff, M., Cheng, C., 2013. A multi-mechanism model for cutting simulations combining visco-plastic asymmetry and phase transformation. Int. J. Solids Struct. 50, 3045–3066. https://doi.org/10.1016/j.ijsolstr.2013.05.008.

Mahnken, R., Wolff, M., Schneidt, A., Böhm, M., 2012. Multi-phase transformations at large strains – thermodynamic framework and simulation. Int. J. Plast. 39, 1–26.

https://doi.org/10.1016/j.ijplas.2012.05.009.

Malvern, L.E., 1969. Introduction to the Mechanics of a Continuous Medium. Prentice-Hall, Inc., Englewood Cliffs.

Mamivand, M., Zaeem, M.A., Kadiri, H.E., 2014. Shape memory effect and pseudoelasticity behavior in tetragonal zirconia polycrystals: a phase field study. Int. J. Plast. 60, 71–86. https://doi.org/10.1016/j.ijplas.2014.03.018.

Nishimura, F., Liedl, U., Werner, E., 2003. Simulation of martensitic transformations in TRIP-steel and Fe-based shape memory alloy. Comput. Mater. Sci. 26, 189–196. https://doi.org/10.1016/S0927-0256(02)00398-1.

Nishimura, F., Tanaka, K., 1998. Phenomenological analysis of thermomechanical training in an Fe-based shape memory alloy. Comput. Mater. Sci. 12, 26–38. https://doi.org/10.1016/S0927-0256(98)00017-2.

Nishimura, F., Watanabe, N., Tanaka, K., 1996. Transformation lines in an Fe-based shape memory alloy under tensile and compressive stress states. Mater. Sci. Eng. 221, 134–142. https://doi.org/10.1016/S0921-5093(96)10486-X.

Nishimura, F., Watanabe, N., Tanaka, K., 1997a. Analysis of uniaxial stress-strain-temperature hysteresis in an Fe-based shape memory alloy under thermomechanical loading. Comput. Mater. Sci. 8, 349–362. https://doi.org/10.1016/S0927-0256(97)00050-5.

Nishimura, F., Watanabe, N., Tanaka, K., 1997b. Hysteretic behavior in an Fe-based shape memory alloy under tensile/compressive cyclic thermomechanical loading. J. Soc. Mater. Sci. 46, 23–30. https://doi.org/10.2472/jsms.46.3Appendix_23.

Ojha, A., Sehitoglu, H., 2016. Transformation stress modeling in new FeMnAlNi shape memory alloy. Int. J. Plast. 86, 93–111. https://doi.org/10.1016/j.ijplas.2016.08.003.

Olson, G., Cohen, M., 1972. A mechanism for the strain-induced nucleation of martensitic transformations. J. Less Common Met. 28, 107–118. https://doi.org/10.1016/0022-5088(72)90173-7.

Peultier, B., Ben Zineb, T., Patoor, E., 2006. Macroscopic constitutive law of shape memory alloy thermomechanical behaviour. Application to structure computation by FEM. Mech. Mater. 38, 510–524. https://doi.org/10.1016/j.mechmat.2005.05.026.

Sato, A., Chishima, E., Soma, K., Mori, T., 1982. Shape memory effect in $\gamma \leftrightarrows \varepsilon$ transformation in Fe-30Mn-1Si alloy single crystals. Acta Metall. 30, 1177–1183. https://doi.org/10.1016/0001-6160(82)90011-6.

Sawaguchi, T., Kikuchi, T., Kajiwara, S., 2005. The pseudoelastic behavior of Fe–Mn–Si-based shape memory alloys containing Nb and C. Smart Mater. Struct. 14, 317–322. https://doi.org/10.1088/0964-1726/14/5/022.

Sidoroff, F., Dogui, A., 2001. Some issues about anisotropic elastic–plastic models at finite strain. Int. J. Solids Struct. 38, 9569–9578. https://doi.org/10.1016/S0020-7683(01)00139-1.

Taylor, G., 1938. Plastic strain in metals. J. Inst. Met. 62, 307–324.

Tjahjanto, D.D., Turteltaub, S., Suiker, A.S.J., 2008. Crystallographically based model for transformation-induced plasticity in multiphase carbon steels. Continuum Mech. Therm. 19, 399–422. https://doi.org/10.1007/s00161-007-0061-x.

Torra, V., Isalgue, A., Lovey, F.C., Sade, M., 2015. Shape memory alloys as an effective tool to damp oscillations. J. Therm. Anal. Calorim. 119, 1475–1533. https://doi.org/10.1007/s10973-015-4405-7.

Vladimirov, I.N., Pietryga, M.P., Reese, S., 2010. Anisotropic finite elastoplasticity with nonlinear kinematic and isotropic hardening and application to sheet metal forming. Int. J. Plast. 26, 659–687. https://doi.org/10.1016/j.ijplas.2009.09.008.

Wang, G., Peng, H., Sun, P., Wang, S., Wen, Y., 2016. Effect of titanium addition on shape memory effect and recovery stress of training-free cast Fe–Mn–Si–Cr–Ni shape memory alloys. Mater. Sci. Eng. 657, 339–346. https://doi.org/10.1016/j.msea.2016.01.099.

Wang, J., Moumni, Z., Zhang, W., Xu, Y., Zaki, W., 2017. A 3D finite-strain-based constitutive model for shape memory alloys accounting for thermomechanical coupling and martensite reorientation. Smart Mater. Struct. 26, 1–15. https://doi.org/10.1088/1361-665X/aa6c17.

Wei, X., Fu, R., Li, L., 2007. Tensile deformation behavior of cold-rolled TRIP-aided steels over large range of strain rates. Mater. Sci. Eng. 465, 260–266. https://doi.org/10.1016/j.msea.2007.02.126.

Wen, Y., Peng, H., Raabe, D., Gutierrez-Urrutia, I., Chen, J., Du, Y., 2014. Large recovery strain in Fe-Mn-Si-based shape memory steels obtained by engineering annealing twin boundaries. Nat. Commun. 5, 1–9. https://doi.org/10.1038/ncomms5964.

Xiao, H., 2014. An explicit, straightforward approach to modeling SMA pseudoelastic hysteresis. Int. J. Plast. 53, 228–240. https://doi.org/10.1016/j.ijplas.2013.08.010.

Xu, R., Bouby, C., Zahrouni, H., Ben Zineb, T., Hu, H., Potier-Ferry, M., 2018. A multiscale analysis on the superelasticity behavior of architected shape memory alloy materials. Materials 11, 1–19. https://doi.org/10.3390/ma11091746.

Xue, G., Zhang, P., Li, X., He, Z., Wang, H., Li, Y., Ce, R., Zeng, W., Li, B., 2018. A review of giant magnetostrictive injector (GMI). Sens. Actuators A Phys. 273, 159–181. https://doi.org/10.1016/j.sna.2018.02.001.

Zaki, W., Moumni, Z., 2007. A three-dimensional model of the thermomechanical behavior of shape memory alloys. J. Mech. Phys. Solids 55, 2455–2490. https://doi.org/10.1016/j.jmps.2007.03.012.